

FEBRUARY 2025

M.Sc. in Electrical and Electronics Engineering

ALIYU GARBA IBRAHIM

**REPUBLIC OF TÜRKİYE
GAZİANTEP UNIVERSITY
GRADUATE SCHOOL OF NATURAL & APPLIED SCIENCES**

**COMPARISON OF ENERGY STORAGE SYSTEMS FOR
FREQUENCY REGULATION**

**M.Sc. THESIS
IN
ELECTRICAL AND ELECTRONICS ENGINEERING**

**BY
ALIYU GARBA IBRAHIM
FEBRUARY 2025**

**COMPARISON OF ENERGY STORAGE SYSTEMS FOR
FREQUENCY REGULATION**

M.Sc. Thesis

in

Electrical and Electronics Engineering

Gaziantep University

Supervisor

Prof. Dr. Ahmet Mete VURAL

by

Aliyu Garba IBRAHIM

February 2025



©2025[Gaziantep University]

**COMPARISON OF ENERGY STORAGE SYSTEMS FOR FREQUENCY
REGULATION**

Submitted by **Aliyu Garba IBRAHIM** in partial fulfillment of the requirements for the degree of master of science in **Electrical and Electronics Engineering, Gaziantep University** is approved by,,

Prof. Dr. Çiğdem AYKAÇ
Director of the Graduate School of Natural and Applied Sciences

Prof. Dr. Ergun ERÇELEBİ
Head of the Department of Electrical and Electronics Engineering

Prof. Dr. Ahmet Mete VURAL
Supervisor, Electrical and Electronics Engineering
Gaziantep University

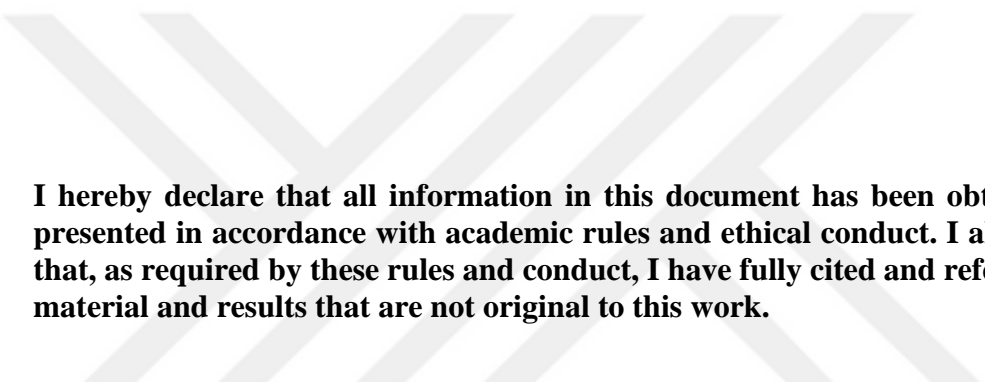
Exam Date: 4th Febuary, 2025

Examining Committee Members:

Prof. Dr. Ahmet Mete VURAL
Gaziantep University

Assist. Prof. Dr. Ali Osman ARSLAN
Gaziantep University

Assist. Prof. Dr. Hasan A M ABUMETEIR
Gaziantep Islam Science and Technology University



I hereby declare that all information in this document has been obtained and presented in accordance with academic rules and ethical conduct. I also declare that, as required by these rules and conduct, I have fully cited and referenced all material and results that are not original to this work.

Aliyu Garba IBRAHIM

ABSTRACT

COMPARISON OF ENERGY STORAGE SYSTEMS FOR FREQUENCY REGULATION

Aliyu Garba, IBRAHIM

M.Sc. in Electrical and Electronics Engineering

Supervisor: Prof. Dr. Ahmet Mete VURAL

February 2025

72 pages

This thesis explores the modeling, analysis, and control of single-area and two-area power systems to enhance frequency regulation amid growing renewable energy integration. Load frequency control mechanisms are investigated to minimize frequency deviations and optimize overall system performance. The dynamic behavior of photovoltaic and wind energy systems is analyzed, along with energy storage technologies such as battery energy storage systems, flywheel energy storage systems, and superconducting magnetic energy storage systems, to enhance grid stability. To improve frequency control, three metaheuristic optimization algorithms (whale optimization algorithm, lightning search algorithm, and artificial rabbit optimization) are employed for PID controller tuning. Simulation results demonstrate that artificial rabbit optimization provides superior frequency stabilization, reduced oscillations, and improved tie-line power compensation under varying load and renewable energy disturbances compared to the other optimization methods. While the integration of energy storage systems enhances transient stability, it introduces a trade-off in the form of increased system settling time. The findings underscore the effectiveness of optimized PID control and energy storage system deployment in achieving stable and resilient power system operation.

Key words: Battery Energy Storage System, Battery Energy Storage System, Renewable Energy, Artificial Rabbit Optimization, Lightning Search Optimization Algorithm, Whale Optimization Algorithm.

ÖZET

FREKANS REGÜLASYONU İÇİN ENERJİ DEPOLAMA SİSTEMLERİNİN KARŞILAŞTIRILMASI

Aliyu Garba, İBRAHİM

Yüksek Lisans Tezi, Elektrik-Elektronik Mühendisliği

Danışman: Prof. Dr. Ahmet Mete VURAL

Şubat 2025

72 sayfa

Bu tez, artan yenilenebilir enerji entegrasyonu bağlamında frekans düzenlemesini iyileştirmek amacıyla tek alanlı ve iki alanlı güç sistemlerinin modellenmesi, analizi ve kontrolünü incelemektedir. Frekans saptamalarını en aza indirmek ve genel sistem performansını optimize etmek için yük-frekans kontrol mekanizmaları araştırılmıştır. Fotovoltaik ve rüzgâr enerji sistemlerinin dinamik davranışları analiz edilmiş, ayrıca şebeke kararlılığını artırmak amacıyla batarya enerji depolama sistemleri, volan enerji depolama sistemleri ve süperiletken manyetik enerji depolama sistemleri gibi enerji depolama teknolojileri incelenmiştir. Frekans kontrolünü iyileştirmek amacıyla, PID denetleyicisinin parametre ayarı için üç meta-sezgisel optimizasyon algoritması (balina optimizasyon algoritması, yıldırım arama algoritması ve yapay tavşan optimizasyonu) kullanılmıştır. Simülasyon sonuçları, yapay tavşan optimizasyonunun diğer optimizasyon yöntemleriyle karşılaştırıldığında daha üstün frekans stabilizasyonu, azaltılmış salınımlar ve değişen yük ile yenilenebilir enerji bozulmaları altında iyileştirilmiş hatlar arası güç dengelemesi sağladığını göstermiştir. Enerji depolama sistemlerinin entegrasyonu geçici kararlılığı artırsa da, sistem yerleşme süresinin uzaması şeklinde bir ödün meydana getirmektedir. Elde edilen bulgular, optimize edilmiş PID kontrolü ve enerji depolama sistemlerinin kullanımının, kararlı ve dayanıklı bir güç sistemi işletimi sağlama açısından etkinliğini vurgulamaktadır.

Anahtar Kelimeler: Batarya Enerji Depolama Sistemi, Volan, Süperiletken Manyetik, Yenilenebilir Enerji, Yapay Tavşan Optimizasyonu, Yıldırım Arama Algoritması, Balina Optimizasyonu.



‘Dedicated to my family’

ACKNOWLEDGEMENTS

All thanks are due to Allah, the Mighty and Majestic, in whose divine omnipotence has made successful completion of this thesis possible. After that, I would like to extend my deepest gratitude to my supervisor, Prof. Dr. Ahmet Mete VURAL, whose profound expertise, invaluable guidance, constructive feedback, unique perseverance, and prompt responses to emails made this research journey insightful and rewarding. I feel incredibly privileged to have had the opportunity to learn under his tutelage.

Last not the list, my sincere and solid appreciation to my family especially my wife, whose support has been truly instrumental. Having such a remarkable person by my side through countable days and nights has been indeed a divine gift. I am so blessed!

TABLE OF CONTENTS

	Page
ABSTRACT	i
ÖZET	ii
DEDICATION	iii
ACKNOWLEDGEMENTS	iv
TABLE OF CONTENTS	v
LIST OF TABLES	viii
LIST OF FIGURES	ix
LIST OF SYMBOLS	xi
LIST OF ABBREVIATIONS	xiv
CHAPTER 1 INTRODUCTION	1
1.1 Motivation of Study.....	1
1.2 Aim of Thesis and Contributions	2
1.3 Layout of Thesis	3
CHAPTER 2 LITERATURE REVIEW	5
2.1 Introduction	5
2.2 Architecture of Single-Area System.....	5
2.3 Architecture of the two-area system.....	5
2.4 Conclusion.....	7
CHAPTER 3 RESULTS AND DISCUSSION	8
3.1 Introduction	8
3.2 Photovoltaic (PV)	8
3.3 Wind Turbine	10
3.4 Conclusion.....	11
CHAPTER 4 ENERGY STORAGE SYSTEMS	12
4.1 Introduction	12
4.2 ESS 12	
4.2.1 BESS	12

4.2.2 FESS	13
4.2.3 SMESS.....	15
4.3 Conclusion.....	17
CHAPTER 5 CONCLUSIONS	18
5.1 Introduction	18
5.2 Whale Optimization Algorithm.....	18
5.2.1 Mathematical Model and Optimization Algorithm.....	18
5.2.2 Search for Prey Exploration.....	20
5.3 Lightning Search Algorithm.....	22
5.3.1 Properties of Projectiles	23
5.4 Artificial Rabbit Optimization.....	26
5.4.1 Exploration.....	27
5.4.2 Exploitation (Random Hiding)	28
5.4.3 Energy Shrink (switch from exploration to exploitation).....	29
5.5 Conclusion.....	30
CHAPTER 6 SIMULATION RESULT AND DISCUSSION.....	32
6.1 Introduction	32
6.1.1 Case 1.....	32
6.1.2 Case 2.....	33
6.1.3 Case 3.....	35
6.1.4 Case 4.....	36
6.1.5 Case 5.....	38
6.1.6 Case 6.....	43
6.1.7 Case 7.....	46
6.1.8 Case 8.....	49
6.1.9 Case 9.....	53
6.2 Conclusion.....	56
CHAPTER 7 CONCLUSION	58
7.1 Summary of Contributions	58
7.2 Future Expectations	59

REFERENCES	60
APPENDIX	66
CURRICULUM VITAE	70



LIST OF TABLES

	Page
Table 6.1. Optimization results for PID parameters for single-area system under constant wind speed	35
Table 6.2. Optimization results for PID parameters for single-area system under constant irradiation and constant wind speed.....	36
Table 6.3. Parameters of the two-area systems	38
Table 6.4. Comparison of ESS performances on the two-area system	40
Table 6.5. Comparison of power output parameters due to ESS.....	42
Table 6.6. Comparison of optimized parameters for the two-area system under constant RES	44
Table 6.7. Parameters due to optimizations under variable load and ESS in both areas.....	49
Table 6.8. Comparison of Energy storage performance in Area-1.....	54
Table 6.9. Comparison of Energy storage performance in Area-2.....	54

LIST OF FIGURES

	Page
Figure 2.1. Transfer function representation of the single-area power system.....	5
Figure 2.2. Transfer function representation of the two-area power system.....	7
Figure 3.1. The photovoltaic single-diode model of a solar cell [15]	9
Figure 3.2. PV system [14].....	10
Figure 4.1 Overview of FESS in domestic application [25]	14
Figure 5.1. A bubble-net feeding behavior of the humpback whales.[23].....	19
Figure 5.2. Pseudocode of the WOA algorithm [23]	22
Figure 5.3. Step leaders descending from a thundercloud [30].....	22
Figure 5.4. Pseudocode of the LSA.[30].....	26
Figure 5.5. A rabbit net with several burrows [31]	27
Figure 5.6. General steps to apply ARO [33].....	30
Figure 6.1. Comparison of the system’s change in frequency with and without PID controller	33
Figure 6.2. Comparison of the power output of the system with and without PID controller	33
Figure 6.3. Transfer function representation of the single-area system with PV and WT integration	34
Figure 6.4. The disturbances used as input to the system	34
Figure 6.5. Comparison of ARO, LSA, and WOA under constant WT and variable load.....	35
Figure 6.6. Comparison of ARO, WOA, and LSA under constant RES in a single– area system	36
Figure 6.7. White noise is used as a variation in the speed of WT	37
Figure 6.8. Comparison of ARO, LSA, and WOA under severe disturbances.....	37
Figure 6.9. Frequency deviation of the system tested under different load surges in Areas 1-2	39
Figure 6.10. The power output produced by the two areas and the tie line	39

Figure 6.11. Comparison of the frequency deviation in Area-1 due to the ESS.....	41
Figure 6.12. Comparison of frequency deviation in Area-2 due to ESS.....	41
Figure 6.13. The power output due to ESS at Area-1	42
Figure 6.14. The power output due to ESS in Area-2.....	43
Figure 6.15. The tie-line steady-state power output due to the ESSs.....	43
Figure 6.16. Renewable energy penetration with a constant input in both areas.....	45
Figure 6.17. The frequency deviation of Area-1 under constant PV, WT, and variable load	46
Figure 6.18. Comparison of frequency deviation of Area-2 under constant PV, WT, and no load	46
Figure 6.19. Integration of RES into the System model in both areas and Load disturbance in Area-1	47
Figure 6.20. The disturbances applied to the system	48
Figure 6.21. Comparison of frequency deviation optimizations in Area-1.....	48
Figure 6.22. Comparison of frequency deviation optimizations in Area-2.....	49
Figure 6.23. Frequency deviation comparison under LSA on charging and discharging of FESS.....	50
Figure 6.24. Frequency deviation comparison under WOA on charging and discharging of FESS.....	51
Figure 6.25. Frequency deviation comparison under ARO on charging and discharging of FESS.....	51
Figure 6.26. Frequency deviation comparison under LSA on charging and discharging of FESS.....	52
Figure 6.27. Frequency deviation comparison under WOA on charging and discharging of FESS.....	52
Figure 6.28. Frequency deviation comparison under ARO on charging and discharging of FESS.....	53
Figure 6.29. Simulink model of two-area system integrated with RES and ESSs....	55
Figure 6.30. Energy storage systems comparison in terms of frequency deviation in Area-1&2.....	56

LIST OF SYMBOLS

ρ	air density
k_i	area bias
σ_{batt}	BESS setting droop
β	blade angle
K	Boltzmann's constant
\vec{V}_i	candidate position
ΔP_{12}	changes in power output
I_c	charging current
'V'	coefficient vectors
R_e	coil resistance
F_i	constant ionization rate
ΔE_{disp}	conventional energy supply
P_d	daily power demand
I	DC current flowing through the coil
t	denotes the current iteration
q	electric charge on an electron
E_i^{sl}	energy of the step leader
$T_{1/c}$	filter time constant
v_p	final velocity
P_s	flywheel power evolution
B_1	frequency bias factor
H	generator inertia
T_g	governor time constant
P_g	grid power supply
n	Ideality factor
L	inductance
E_d	inductor voltage

I_{do}	initial value of the inductor's current
v_0	initial velocity
S	integrator operator
T_{in}	inverter dynamic reaction
h	length
Z	load impedance
ρ	mass density
I	moment of inertia
p_i	original projectiles
r_0	outer diameter
E_1	output voltage of the generator
ϕ_{12}	phase angle difference between generators
$\vec{x}_j(t)$	position of iteration
$C_p(\lambda, \beta)$	power coefficient
D	proportionality constant
\vec{R}_{rand}	random position vector
\vec{a}	random vector
\vec{r}	random vector
$R_o C_o F$	Rate of change of frequency
P_{bess}	rated power of the BESS
ΔE_{ref}	reference energy value
I_0	reverse saturation
A_{rotor}	rotor area
R_s	series resistance
R_{sh}	shunt resistance
c	speed of light
R	speed regulation
T_{pv}	speed response of the PV system
T_{FESS}	speed response time constant
s_i^l	step leader
l	stochastic number
P_s	synchronizing power coefficient

T	temperature in kelvin
r_1	three random numbers
X_{12}	tie-line reactance
T_t	time constant
T_{BESS}	time constant of BESS
T_d	time delay
α^T	tip energy
λ	tip speed ration
V	voltage across the coil
V_{ws}	wind speed



LIST OF ABBREVIATIONS

AC	Alternate Current
ACE	Area Control Error
ARO	Artificial Rabbit Optimization
DC	Direct Current
ESS	Energy Storage System
GA	Genetics Algorithm
IGBT	Insulated-Gate Bipolar Transistor
LC	Low Pass
LFC	Load Frequency Control
LSA	Lightning Search algorithm
PCS	Power Conversion System
PDF	Probability Density Function
PID	Proportional Integral Differential
PSO	Particle Swarm Optimization
PV	Photovoltaic
RES	Renewable Energy Source
SOC	State of Charge
VSC	Voltage Source Converter
WOA	Whale Optimization Algorithm
WT	Wind turbine

CHAPTER 1

INTRODUCTION

1.1 Motivation of Study

The escalating integration of renewable energy sources (RES) into power grids has underscored the critical need for efficient and cost-effective energy storage solutions. Battery Storage systems (BESS), particularly those utilizing lithium-ion technology, have emerged as pivotal in addressing the intermittency of renewables, thereby enhancing grid stability and reliability. Recent advancements have significantly bolstered the economic viability of BESS. Notably, lithium-ion battery pack prices plummeted by 20% in 2024, reaching a record low of \$115 per kilowatt-hour. This decline is attributed to manufacturing overcapacity, economies of scale, and the widespread adoption of cost-effective lithium iron phosphate (LFP) batteries [1]. Concurrently, substantial investments are being channeled into energy infrastructure. For instance, TotalEnergies has committed €160 million towards six new battery storage projects in Germany, cumulatively offering 221 megawatts of storage capacity. This initiative is integral to establishing a comprehensive electricity value chain in the region [2].

Advanced control strategies and optimization algorithms are necessary to mitigate frequency deviations when the power systems are faced with various disturbances such sudden load variation, fault, and unpredictable RES generation. ESS provides frequency regulation by dynamically injecting/absorbing power to/from the grid in response to a decrease/increase in frequency. Due to fast response time, ESS technology can inject large amounts of power into the grid in the shortest period, which can be used as virtual inertia. The two most important aspects related to applying fast responsive energy storage technologies for frequency regulation services that is control and sizing are discussed in detail for both single and hybrid storage technologies [3]. In the literature, frequency regulation studies are multifaceted in terms of the type of RES used, the type of controller, and the kind of system disturbance [4]. In [5], an adaptive control strategy to coordinate the

generator and the governor with an ESS in frequency regulation has been proposed. The comparison between the ESS compensation with a conventional droop control and the proposed method has been done. The simulation results show that compared to the ESS with a fixed droop control scheme, the proposed control scheme provides better results in regulating the frequency response by lowering the rate of change of frequency and improving the minimum frequency deviations during the generator tripping events. In [6] the effectiveness of flywheel energy storage system (FESS) in providing primary frequency control has been addressed when applied to a weak grid system. The SOC restoration logic has been considered to ensure service continuity and effective frequency regulation. The optimal size of BESS installation to accomplish the goal has also been studied with a dynamic grid model. Research and inventions have been overflowing in the conventional PI and PID types of controllers and their parameter optimization in power systems. The PID controller is tuned using different optimization methods with comparison and a novel GA-fuzzy logic self-tuning technique is suggested. Results show the suggested method outperforms others in restoring power system stability [7]. The study published in [8] suggests a bat-inspired optimization algorithm that is modeled on an animal's echolocation behavior. This optimization approach is used to enhance load-frequency control (LFC) in a two-area power system with superconducting energy storage system (SMES) unit. [9] Introduces the Gravitational Search Algorithm and Bat-inspired Algorithm as two techniques for designing a model predictive controller for LFC. The power system is embedded with SMES and compressive energy storage. The study [10] introduces the Gravitational Search Algorithm and Bat-inspired Algorithm as two techniques for designing a model predictive controller for LFC. The power system is embedded with SMES and compressive energy storage. The study [11] proposes a hybrid Firefly-particle swarm optimization (PSO) technique to tune PID controller parameters for minimizing frequency deviation in a microgrid under varying wind speeds and load demands. Comparative analysis with PSO and Firefly algorithms has been carried out using various performance indices.

1.2 Aim of Thesis and Contributions

In this thesis, the design and simulation of a single-area system as well as the two-area system is done. The thesis introduces both the design and configuration of these test systems. The thesis aims to comprehend the control strategies employed in the

literature and propose alternatives that would give top-notch mitigation. In addition, it aims to compare and study the performance of ESSs concerning frequency regulation.

Amongst the contributions, this thesis offers to the field of power system stability; the major ones are listed below:

- LFC of single-area and two-area test systems to achieve a high level of stability and robustness due to penetration of RES such as PV and WT is realized.
- The contribution of FESS, BESS, and SMESS in the LFC is evaluated by comparison.
- The comparison of optimization methods such as ARO, LSA, and WOA in enhancing the controller parameters for effective mitigation of frequency instability during severe disturbances is carried out.

1.3 Layout of Thesis

This thesis is composed of seven chapters, including the introductory. The content of the remaining chapters is arranged as follows:

Chapter 2 provides the transfer function model of single-area and two-area systems. The LFC of the two systems are highlighted and their mathematical interpretations.

Chapter 3 brings about detailed information on RES such as PV and WT, the transfer functions, mathematical models, and their interpretations.

Chapter 4 discusses ESSs, the role they play in power system stability. The mathematical models are presented as well as their transfer functions

Chapter 5 introduces the optimization methods, their history, and the details information about the formation of mathematical equations on every stage of the algorithm development.

Chapter 6 provides the simulation analysis and the discussion of the results on a case basis. Each of these cases is discussed separately then a conclusion is made for each.

Chapter 7 is a comprehensive conclusion of everything discussed, a summary of the contribution driven by the work, and the future focus suggestion.



CHAPTER 2

LITERATURE REVIEW

2.1 Introduction

In this chapter, the single-area system is broadly discussed. The configuration setting that shows an effective feedback system is portrayed, and the parameters of every block are presented. An extension of the single-area to the two-area system is made by introducing a tie-line. The mathematical module is first discussed, and then the transfer function block of the entire system is presented.

2.2 Architecture of Single-Area System

The transfer function model of the single-area power system is illustrated in Figure 2.1. The generator inertia constant is defined by $H=5$. The turbine acts as the mechanical power source with its dynamics defined by a time constant $T_t=0.5s$. The governor with the time constant, $T_g=0.2 s$ detects speed changes and modulates the turbine input to restore the steady-state operation. The governor's typical speed regulation is defined as $R=20$, the percentage change of speed from no-load to full-load. The inertia load, incorporating both rotating masses and the connected load is quantified by the proportionality constant $D=0.8$, which represents the percentage change in load per percentage change in frequency [12].

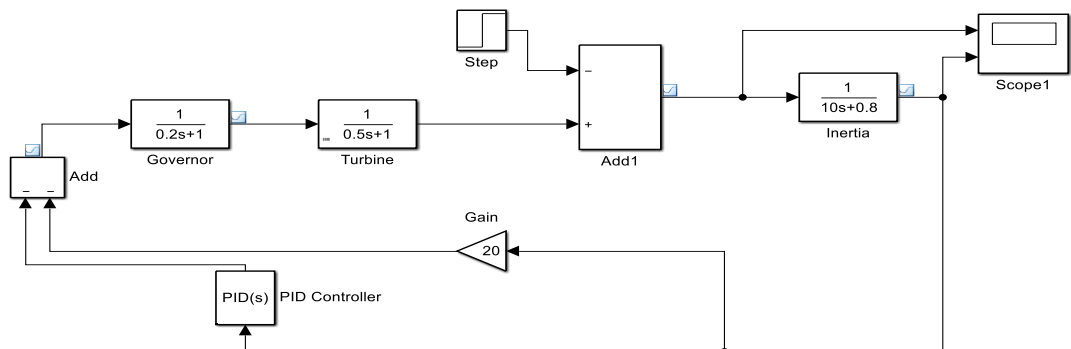


Figure 2.1. Transfer function representation of the single-area power system

2.3 Architecture of the two-area system

The Two-area power system is usually modeled as two separate generation locations, each of which is modeled using an ideal AC voltage source and a reactance

connected in series. Then, the outputs of these locations are connected with a tie line. In this way, the steady-state behavior of this system can be modeled in its simplest form. The tie-line active power flow from area-1 to area-2 when neglecting losses can be calculated.

$$P_{12} = \frac{|E_1||E_2|}{X_{12}} \sin\phi_{12} \quad (2.1)$$

where, E_1 and E_2 respectively represents the output voltage of each generator, X_{12} is the tie-line reactance, and ϕ_{12} is the phase angle difference between each generator output. The tie line power deviation is represented by equation 2.2, which is perceived as an increase in load in one area and a corresponding decrease in the other, depending on the flow's direction. This direction is determined by the change in phase angle difference between the two areas. For instance, if $\Delta\phi_1 - \Delta\phi_2$ is positive, the active power flows from area 1 to 2. P_s is the synchronizing power coefficient. The conventional LFC relies on tie-line bias control as shown in equation 2.3, where each control area aims to minimize the area control error (ACE) to zero. The ACE in each area is a combination of frequency deviation and tie-line power flow error represented as below.

$$\Delta P_{12} = P_s (\Delta\phi_1 - \Delta\phi_2) \quad (2.2)$$

$$ACE_i = \sum_{j=1}^n \Delta p_{ij} + k_i \Delta f \quad (2.3)$$

The area bias k_i determines the level of interaction between neighboring areas during a disturbance. Optimal performance is achieved when k_i is set to the frequency bias factor of that area, $B_i = \beta_i + D_i$. For a two-area system, the ACE equations are given as:

$$ACE_1 = \Delta P_{12} + B_1 \Delta F_1 \quad (2.4)$$

$$ACE_2 = \Delta P_{21} + B_2 \Delta F_2 \quad (2.5)$$

B_1 and B_2 are known as frequency bias factors, ΔP_{12} and ΔP_{21} are changes in power output in both areas. Each area is modeled with an equivalent turbine and governor, and the incremental power balance is controlled by the tie-line bias control which is

the ACE. The synchronizing power coefficient P_s is taken as 2.0 p.u. The transfer function representation of the two-area power system is depicted in Figure 2.2.

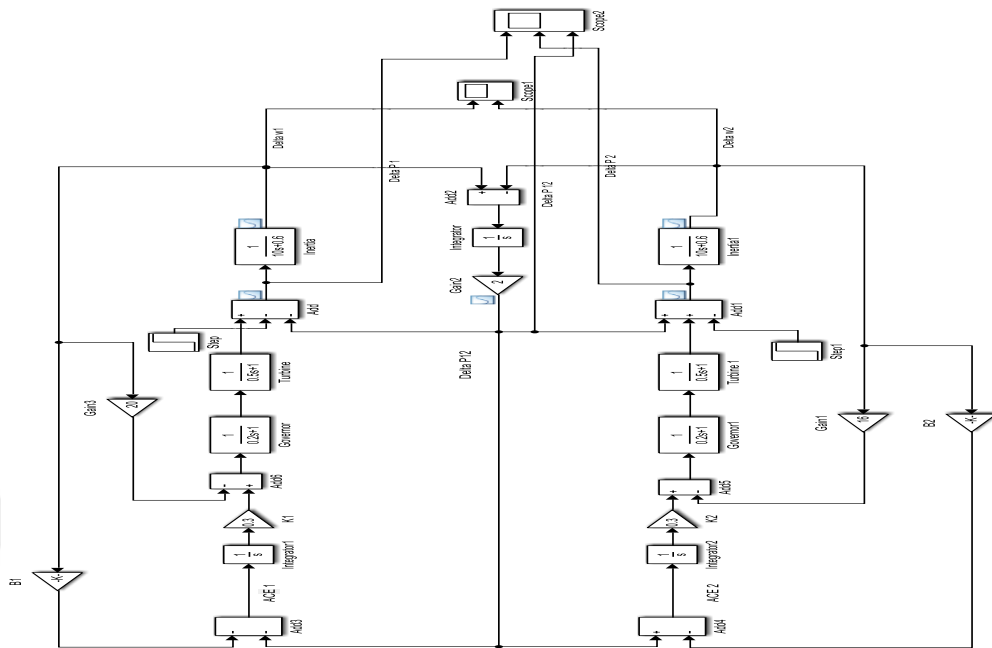


Figure 2.2. Transfer function representation of the two-area power system

2.4 Conclusion

This chapter presented the modeling and analysis of single-area and two-area power systems, focusing on their dynamics behavior and load frequency control (LFC) mechanisms. The single-area system was described using a transfer function model, incorporating key parameters such as governor response, turbine dynamics, and system inertia. The role of the governor in detecting speed changes and regulating the turbine input to maintain system stability was highlighted, with parameters such as speed regulation (R) and frequency sensitivity (D) playing a crucial role in system response. For the two -area power system, the tie-line interconnection was analyzed, demonstrating its impact on active power exchange and frequency stability. The mathematical formulation of tie-line power flow and the area control error (ACE) was presented, showing how LFC minimizes deviations in frequency and inter-area power exchange. The importance of frequency bias factors in optimizing system performance was also discussed.

CHAPTER 3

RESULTS AND DISCUSSION

3.1 Introduction

In this chapter, essential information on PV is presented, and the circuitry analysis of panel components is elaborated. The control and conversion part of the integration process is widely discussed. Equations of the mathematical models of PV and the transfer function are presented

3.2 Photovoltaic (PV)

PV is one of the leading RES due to its simplicity, reliability, and economic advantage compared to other renewable sources. Tremendous research has been done in many aspects of PV, ranging from design, control, integration, model parameters configuration, and above all, economic constraint. Generally, the performance of a PV cell in any climatic condition rests on the five equations of a single diode model illustrated in Figure 3.1, and these equations give values to the five parameters [13]. Each of these parameters contributes to the quality and stability of the output performance of the PV as it is critically proven in this [14] that one of the five parameters, the shunt resistance plays a significant role in the operating characteristics of a solar PV array, when the temperature drops, its value reduces from 1000 ohms to 0.1 ohms. Hence, output power and voltage increase slightly. In the same context, the five parameters can be determined using three cardinal points as elaborated in this research [15], namely the open-circuit point ($V_{oc}, 0$), maximum power point (V_{mp}, I_{mp}), and the short-circuit point ($0, I_{sc}$).

$$I = I_L - I_0 \left(e^{\left(\frac{q(V+IR_s)}{nKT} \right)} - 1 \right) - \frac{V + IR_s}{R_{sh}} \quad (3.1)$$

$$I_{sc} = I_L - I_0 \left(e^{\left(\frac{qI_{sc}R_s}{nKT} \right)} - 1 \right) - \frac{I_{sc}R_s}{R_{sh}} \quad (3.2)$$

$$0 = I_L - I_0 \left(e^{\left(\frac{qV_{oc}}{nKT} \right)} - 1 \right) - \frac{V_{oc}}{R_{sh}} \quad (3.3)$$

$$I_M = I_L - I_0 \left(e^{\left(\frac{q(V_M + I_M R_s)}{nKT} \right)} - 1 \right) - \frac{V_M + I_M R_s}{R_{sh}} \quad (3.4)$$

$$I_M = (V_M - I_M R_s) \left(\frac{I_0 q}{nKT} e^{\left(\frac{q(V + I R_s)}{nKT} \right)} + \frac{1}{R_{sh}} \right) \quad (3.5)$$

Where I is an explicit function of V and vice-versa, I_0 is reverse saturation, K is Boltzmann's constant = 1.6×10^{-23} , T is the temperature in Kelvin, R_{sh} is shunt resistance, and n is the ideality factor, and R_s is series resistance, and q is an electric charge on an electron = 1.6×10^{-19} , I_L = Light generated current, I_M = Maximum current, I_{SC} = short circuit current, V_{OC} = Open circuit voltage, V_M = Maximum voltage.

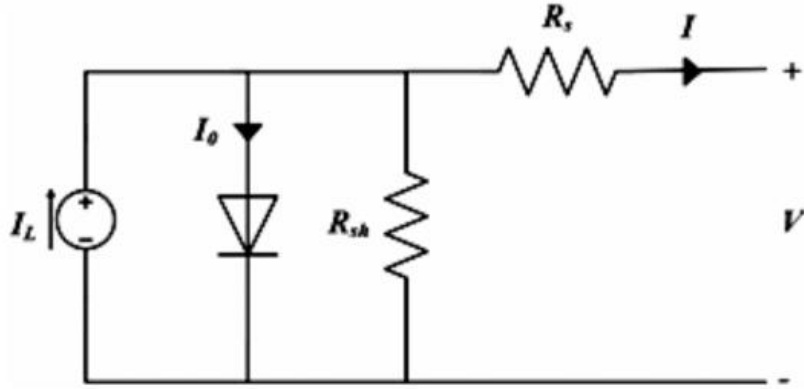


Figure 3.1. The photovoltaic single-diode model of a solar cell [15]

The power output of any PV cell can be determined by evaluating data-driven methods as elaborated in [16] before designing the control system or integration. Amongst these are- Predicting PV module output power based on measured cell temperature and environmental factors such as irradiation on the plane of the array, ambient temperature, and wind velocity, secondly, estimating PV module on the basis of climatic parameters, including irradiation on a horizontal surface or tilted, ambient temperature and wind velocity.

The next stage when the power is generated, is conversion and control from DC to DC and/or from DC to AC before being transmitted into the grid as shown in Figure 3.2. A boost converter produces an output voltage higher than the input received from the solar cell. Its basic circuit comprises two switching semiconductor

components, along with an inductor, a capacitor, and a resistor. [14] the DC to AC inverter includes a converter and $R_F C_F$ filter to minimize the impact of the beat rate of the current on the voltage difference between the grid and the output of the converter and to “smooth” the electric current, transformer, and circuit breaker.

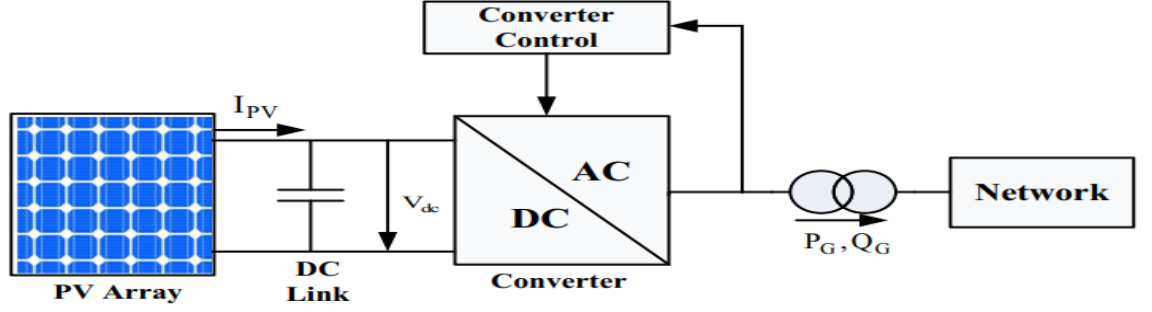


Figure 3.2. PV system [14]

As presented in [7] the PV model can be formulated in three first-order transfer functions. It provides sufficient small signals to capture the power dynamics of the PV. It consists of three blocks- the time-constant T_{pv} indicates the speed response of the PV system, the time-constant T_{in} represents how quickly the inverter dynamics react to changes from the PV system, and $T_{1/c}$ represents a control filter that smooths out the signal from the inverter. The overall transfer functions of PV can be expressed as the product of three transfer functions in equation (3.6).

$$\Delta P_{pv} = \frac{1}{T_{pv}s + 1} \times \frac{1}{T_{in}s + 1} \times \frac{1}{T_{1/c} + 1} \quad (3.6)$$

3.3 Wind Turbine

Fluctuations in wind speed and direction across the rotor influence power generation. The larger the rotor diameters and greater hub heights, the bigger the size of utility-scale turbines as they extend further into the atmospheric boundary layer [17]. Wind power production P_{WT} can be computed using equation 3.7 as a function of wind speed V_{WS} , air density ρ , rotor area A_{rotor} , and power coefficient $C_p(\lambda, \beta)$, with β as a blade angle and λ the tip-speed ratio is given in equation 7 [18],

$$P_{WT} = \frac{1}{2} \rho A_{rotor} C_p(\lambda, \beta) V^3 \quad (3.7)$$

The tip speed of the blade is determined by multiplying the rotor's rotational speed and the rotor's radius. Therefore, we can express the tip-speed ratio as a function of the rotor's rotational speed, the radius, and the wind speed as in equation 3.8.

$$\lambda = \frac{\omega \cdot (D_{rotor}/2)}{V_{ws}} \quad (3.8)$$

The wind turbine is a first-order transfer function presented in equation 3.9 [7]. It shows how the wind turbine's power output responds to dynamics in the input signal. In LFC, this model regulates the active power output, manages the frequency response, and controls the pitch angle or rotor speed of the wind turbine in optimizing the power generation.

$$\Delta P_{WT} = \frac{1}{T_{WT}s + 1} \quad (3.9)$$

3.4 Conclusion

PV and Wind energy systems are among the leading RES due to their reliability, economic advantages, and technological advancements. The performance of a PV system is governed by key parameters derived from the single-diode model, with factors such as shunt resistance playing a significant role in its output characteristics. Proper modelling and control strategies, including transfer function analysis, help optimize PV integration into the power grid. Similarly, wind turbine systems rely on aerodynamic principles, with power output determined by wind speed, rotor size, and power coefficient. Their dynamic behaviour is captured using third and first-order transfer functions, which aid in frequency regulation and active power control. Both PV and wind energy systems require efficient power conversion and control mechanisms, such as boost converters and inverters, to ensure stable and high-quality power injection into the grid. By understanding their operational dynamics and implementing effective control strategies, RES can significantly contribute to grid stability, enhance energy security, and support the transition toward sustainable power generation.

CHAPTER 4

ENERGY STORAGE SYSTEMS

4.1 Introduction

In this chapter, the ESS role in the stability of the power system is discussed. The charge and discharge scenarios are formulated, and the control part of the ESS that encompasses DC to AC conversion is discussed

4.2 ESS

The ESS plays an essential role in power system stability, acting as a temporary energy buffer. They store energy from generation sources and strategically supply it to loads or the grid to achieve key objectives such as balancing supply and demand, load leveling, load shifting, voltage support, frequency regulation, integrating distributed generation, and providing spinning reserve. Various technologies are employed for electricity conversion and storage, categorized by the energy form they utilize- mechanical, electrochemical, chemical, and thermal. A power conversion system (PCS), including an inverter/rectifier, converts the DC voltage from storage to AC voltage for grid compatibility. The PCS is equipped with a set of controllers, that are designed to facilitate specific functions for interfacing the ESS with the power network [19].

4.2.1 BESS

BESS is usually located near a distribution and substation and connected at the point of common coupling. It acts as an energy buffer to temporarily store and deliver energy under specific conditions such as time or load level to achieve the intended objective. The grid primarily supplies the load while charging the battery during off-peak hours or surplus energy periods. BESS discharges during peak demand and serves as emergency backup during grid outages [20]. To size the battery, the reference values for the required regulation energy ΔE_{ref} and the energy potentially supplied by conventional generation units (ΔE_{disp}) must be estimated. The required regulation energy can be estimated from the magnitude of the loss of the generation

group and the frequency's target value to be achieved. The difference between the required and available regulation energy from conventional sources helps define the necessary BESS-rated power using a power balance equation.

$$P_{bess} = \sigma_{batt} f_n (\Delta E_{ref} - \Delta E_{disp}) \quad (4.1)$$

Where P_{bess} is the requested rated power of the BESS, and σ_{batt} is the BESS setting droop [21]. The bi-directional converter connects to the BESS for energy storage and delivery in operating both DC-AC and AC-DC modes. It is designed with an insulated-gate bipolar transistor (IGBT), where few operate as DC-AC converters, and few operate as AC-DC converters. This converter regulates the charge-discharge process through control logic. An LC filter is connected to the three-phase line to remove the unwanted noise from the converter's output [22]. For LFC, ESSs are considered ancillary sources that contribute to frequency stability and droop control. BESS is expressed as a first-order transfer function as in equation 4.2.

$$\Delta P_{BESS} = \frac{1}{T_{BESS} s + 1} \quad (4.2)$$

This is a first-order low-pass filter transfer function, which means that the BESS does not respond instantaneously to power change requests but instead follows a gradual response dictated by T_{BESS} . The smaller the time constant, the faster the response, and vice versa. It smooths out rapid fluctuations by injecting power into the grid [23].

4.2.2 FESS

In this technology, electricity is stored using a motor to convert electrical energy from the power grid or an external source into mechanical energy. The energy stored in the flywheel is a function of the mass density, inner diameter, outer diameter, angular velocity, length, etc. The stored energy can then be converted back into electrical energy by operating the same motor as a generator [24]

The rotational energy stored in the flywheel is defined as

$$E = \frac{1}{2} I \omega^2 \quad (4.3)$$

where I is the moment of inertia directly proportional to the rotor's mass using a constant that depends on the shape factor. ω is the angular velocity. The moment of inertia for the cylinder flywheel is defined as:

$$I = \frac{1}{2}\pi h\rho((r_0)^4 - (r_i)^4) \quad (4.4)$$

where the outer diameter and inner diameter are represented by r_0 and r_i , respectively, h is the length and ρ is the mass density. Hence

$$E = \frac{1}{4}\pi h\rho\omega^2(r_0^4 - r_i^4) \quad (4.5)$$

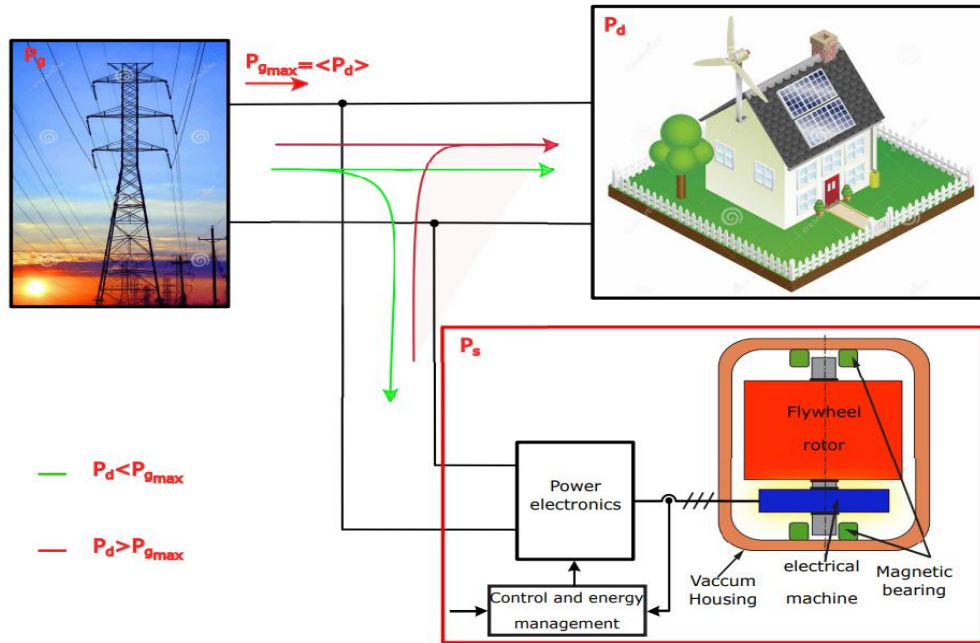


Figure 4.1 Overview of FESS in domestic application [25]

The flywheel used for domestic purposes consists of five key components: a flywheel rotor, magnetic bearings, an electric machine, a power electronic interface, and housing. The system in Figure 4.1, manages daily power demand (P_d), flywheel power evolution (P_s), and grid power supply (P_g). FESS stores excess energy when domestic consumption is low and supplies power during peak demand, helping to limit grid load [25]. FESS is suitable for a wide range of applications, from large power grids to small households. Rather than large-scale manufacturing units, FESS

arrays are typically used to achieve high-power and high-capacity storage, allowing a more flexible power configuration. Key applications include enhancing power quality through grid frequency and wind power smoothing, pulse power applications, high-quality uninterruptible power system supply applications, locomotive energy recovery, and aerospace attitude control [26].

FESS as in [23], T_{FESS} represent the speed of response of the flywheel system to provide or absorb power to maintain system stability

$$\Delta P_{FESS} = \frac{1}{T_{FESS} + 1} \quad (4.6)$$

The time constant indicates how quickly it responds to power fluctuations, FESS is usually recorded with a 10% lower time constant than BESS, hence, 10 times faster response to charging/discharging power. It doesn't deliver instantaneous power but follows a gradual response. Prevent abrupt energy variation.

4.2.3 SMESS

In [27] SMESS is the power conditioning system that manages the power transfer between the superconducting coil and the AC system. Various topologies are available for charging and discharging SMES, including:

- Thyristor-based PCS
- Voltage source converter (VSC)-based PCS

Thyristor-based SMES primarily controls active power with limited reactive power capability, and its active and reactive power controls are not independent. Therefore, in applications in which mainly active power control is required, the thyristor-based SMES is used, while VSC-based SMES is preferred when reactive or combined active and reactive power control is needed. An SMES device operates with DC to store energy in a magnetic field. The DC flowing through a superconducting wire in a large magnet creates the magnetic field. The key specifications for SMES devices typically include inductively stored energy and rated power measured in watts.

$$E = \frac{1}{2} LI^2 \quad (4.7)$$

$$P = \frac{dE}{dt} = LI \frac{dI}{dt} = VI \quad (4.8)$$

where L is the inductance of the coil, I is DC current flowing through the coil, and V is the voltage across the coil. [28] There are three modes of SMES operation: charging, storing, and discharging modes. These modes are expressed mathematically as follows.

4.2.3.1 Charging Mode

The charging current can be expressed as a function of the voltage and impedance of the coil:

$$I_c(t) = \left(\frac{U}{R_e}\right) \left[1 - \exp\left(-\frac{R_e \times t}{L}\right)\right] \quad (4.9)$$

where $I_c(t)$ is the charging current as a function of time, U is the voltage of the source, R_e is the coil resistance and L is the coil inductance. The $V(t)$ across the inductor is expressed as:

$$V(t) = L \frac{dI_c(t)}{d(t)} \quad (4.10)$$

4.2.3.2 Discharging mode

Once the inductor is fully charged, the power supply is disconnected, and the superconductor becomes ready for uncontrolled discharge. Assuming the load impedance Z is purely resistive R , the resulting uncontrolled discharge current is given by equation 11, which represents the discharging current at coil resistance R . When the coil resistance leads to zero, the discharging current can be expressed in equation 4.12.

$$I_{dis}(t) = I_0 \exp\left[-\frac{(R + R_e)t}{L}\right] \quad (4.11)$$

$$I_{dis}(t) = I_0 \exp\left(-\frac{Rt}{L}\right) \quad (4.12)$$

In LFC, SMES is designed as given in [5] based on the following equations:

$$\Delta E_d(s) = \frac{K_d}{T_d s + 1} \quad (4.13)$$

$$\Delta I_d = \frac{E_d}{SL} \quad (4.14)$$

$$\Delta P_{SMES} = I_{do} \times \Delta E_d + \Delta E_d \times \Delta I_d \quad (4.15)$$

where K_d is the gain of the control loop, T_d is the time delay associated with the power system converter as shown in equations 4.13. The deviation in the inductor current can be seen in equation 5, L stands for the inductance of the SMES coil and E_d is the change in the inductor voltage. Finally, the deviation in the SMES unit's power flow and I_{do} is the initial value of the inductor current given in equation 4.15.

4.3 Conclusion

A well-designed energy storage system is essential for maintaining power system stability by acting as a temporary energy buffer. Various technologies, including BESS, FESS, and SMESS, offer different advantages based on their energy storage and power delivery characteristics. BESS provides effective frequency regulation and load management, FESS ensures rapid response to power fluctuations, and SMESS facilitates high-efficiency energy transfer through controlled magnetic fields. Integrating these storage systems with power conversion technologies, such as inverters, bi-directional converters, and thyristor-based controllers, ensures seamless operation within the grid. The mathematical models governing their performance highlight their dynamic response and suitability for different grid applications. Ultimately, the appropriate selection and implementation of energy storage technologies play a critical role in enhancing grid resilience, improving frequency stability, and supporting the integration of RES.

CHAPTER 5 CONCLUSIONS

5.1 Introduction

In this chapter, novel meta-heuristic methods are discussed. The mathematical model of each algorithm is presented step by step with an in-depth analysis. A composed pseudo-code is available for realizing the MATLAB code.

5.2 Whale Optimization Algorithm

A novel and nature-inspired meta-heuristic optimization algorithm that explores and mimics the hunting tactics of an aquatic organism called a whale. Cetaceans, commonly referred to as whales, constitute the largest order of mammals. Adult specimens can attain substantial dimensions, reaching lengths exceeding 30 meters and weights exceeding 180 metric tons. This order encompasses seven recognized major species, including killer whales, minke whales, sei whales, humpback whales, right whales, fin whales, and blue whales. Predation constitutes a primary mode of sustenance for most cetacean species. Due to their obligate air-breathing nature, continuous vigilance is necessary to ensure respiratory function, resulting in a unique form of uni-hemispheric slow-wave sleep. Furthermore, cetaceans are widely regarded as highly intelligent animals exhibiting complex social behaviors and emotional capacities [23].

5.2.1 Mathematical Model and Optimization Algorithm

Following [23], this algorithm is designed on the nature and tactics used by a whale to hunt and can be put into three. Namely, Encircling prey, bubble-net attacking method, and searching for prey [29]. These methodologies were used in designing the algorithm based on the following equations:

5.2.1.1 Encircling the prey

This tactic is formulated and designed based on the following equations:

$$\vec{P} = |\vec{Q} \cdot \vec{R} * (t) - \vec{R}(t)| \quad (5.1)$$

$$\vec{R}(t + 1) = \vec{R} * (t) - \vec{V} \cdot \vec{W} \quad (5.2)$$

where t denotes the current iteration, the vectors ‘V’ and ‘Q’ are coefficient vectors that dynamically adjust throughout the optimization process. ‘R’ represents the position vector of the current best solution within the search space. The operation ‘|’ signifies the absolute value, while ‘.’ Denotes element-wise multiplication. It is crucial to note that the ‘R’ vector must be updated iteratively to reflect the discovery of any superior solutions during the optimization process.

$$\vec{V} = 2\vec{a} \cdot \vec{r} - \vec{a} \quad (5.3)$$

$$\vec{Q} = 2 \cdot \vec{r} \quad (5.4)$$

Where \vec{r} is a random vector, and \vec{a} is linearly decreasing within the iteration from 2 to 0.

5.2.1.2 Bubble-Net Attacking Tactics

Figure 5.1 shows the hunting strategy and this tactic can be categorized into two ways; shrinking encircling or spiral updating position.

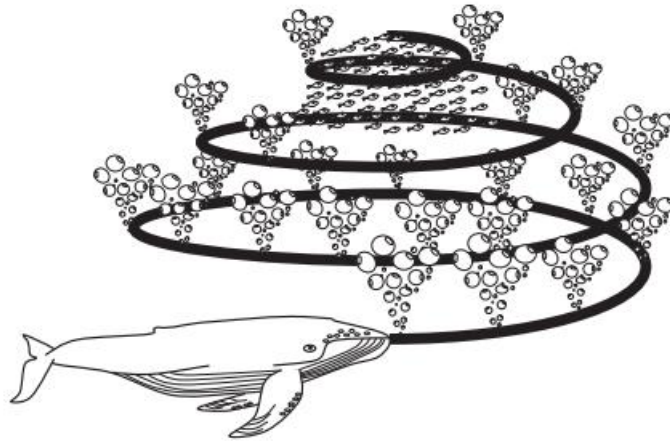


Figure 5.1. A bubble-net feeding behavior of the humpback whales.[23]

5.2.1.3 Shrinking Encircling Tactics

Following [23] this behaviour is achieved by gradually reducing the magnitude of the coefficient vector ‘V’ in equation 17. Concurrently, the range of possible values for ‘V’ is also diminished by a factor of ‘a’ within the interval $[-a, a]$, where the value of ‘a’ decreases linearly from 2 to 0 throughout the iterative process. The search space

is progressively narrowed down by confining the value of ‘a’ within this decreasing range. Consequently, the new position of a search agent can be determined within a region bounded by its original position and the position of the current best solution. The potential positions are within the bounded region for a two-dimensional space. Assuming $0 \leq V \leq 1$.

5.2.1.4 Spiral updating position

Following [23] this tactic is inspired by the unique foraging behavior of humpback whales. This phase involves calculating the Euclidean distance between the current position of the whale (R, Y) and the position of the prey (R, Y). Subsequently, a spiral equation is derived to simulate the helical movement of the whale toward the prey, mirroring the observed behavior of humpback whales during bubble-net feeding.

$$\vec{R}(t + 1) = \vec{W}.e^{bl}.\cos(2\pi l) + \vec{R} * (t) \quad (5.5)$$

where $\vec{P} = |\vec{R} * (t) - \vec{R}(t)|$ and indicate the distance of the i^{th} whale to prey, b is a constant that defines the shape of the spiral, l is a stochastic number in $[-1,1]$, and $*$ is an element-by-element product.

5.2.2 Search for Prey Exploration

Following [23], the exploration phase of the whale optimization algorithm (WOA) leverages variations in the V vector to simulate the process of prey searching. Humpback whales exhibit random search patterns based on their relative positions. In this context, V values greater than 1 or less than -1 are employed to drive search agents away from a reference whale, promoting diverse exploration. Unlike the exploitation phase, where the search agent updates their positions relative to the best solution found, the exploration phase updates based on a randomly selected search agent. This mechanism, combined with the condition $|\vec{V}| > 1$, enhances global search capabilities, ensuring broader exploration of the solution space. The corresponding mathematical model is as follows:

$$\vec{P} = |\vec{Q}.\overrightarrow{R_{rand}} - \vec{R}| \quad (5.6)$$

$$\vec{R}(t + 1) = \overrightarrow{R_{rand}} - \vec{V}.\vec{P} \quad (5.7)$$

Where $\overrightarrow{R_{rand}}$ is a random position vector chosen from the current position. A composed pseudocode that aids in putting the MATLAB code is drafted in Figure 5.2.

```
Initialize the whale population  $R_i (i = 1, 2, \dots, n)$ 
Calculate the fitness of each search agent
 $R^*$  = the best search agent
While ( $t <$  maximum number of iterations)
For each search agent
Update  $a, V, C, l,$  and  $w$ 
If 1 ( $w < 0.5$ )
If 2 ( $|V| < 1$ )
Update the position of the current search by the eq. (5.2)
Else if2 ( $|V| \geq 1$ )
Select a random search agent ( $R_{rand}$ )
Update the position of the current search agent by the eq. (5.7)
End if2
Else if1 ( $w \geq 0.5$ )
Update the position of the current search by the eq.(5.4)
End if1
End for
Check if any search agent goes beyond the search space and
amend it
Calculate the fitness of each search agent
Update  $R^*$  if there is a better solution
 $t = t + 1$ 
end while
```

```
return R*
```

Figure 5.2. Pseudocode of the WOA algorithm [23]

5.3 Lightning Search Algorithm

One of the newest metaheuristic algorithms developed by Shareef in 2015 [30], was crafted from the lightning phenomenon. The application of this method is cast across numerous fields of research and inventions such as computer science, engineering, and mathematics, to mention but a few. The idea of lightning can be attributed to the gaseous atoms, namely nitrogen, oxygen, and hydrogen in the thundercloud. As water molecules freeze within the thundercloud, the parts that cannot incorporate into the lattice, are propelled at high velocities. Imagine these ejected particles as tiny seeds. As they travel through the air, they collide with other molecules, creating a pathway for the lightning bolt to follow. This initial pathway is like the first step in creating the lightning bolt, similar to how the first seeds planted in a field are the starting point for a garden. Figure 5.3 presents the downward display of lightning known as cloud-to-ground flashes.



Figure 5.3. Step leaders descending from a thundercloud [30]

5.3.1 Properties of Projectiles

Following [30], the velocity of the projectile is given in equation 5.8. This describes the speed at which it travels, but the kinetic energy decreases as it collides with atoms and molecules on its path.

$$v_p = [1 - (\frac{1}{\sqrt{1 - (\frac{v_0}{c})^2}} - s \times F_i/m \times c^2)^{-2}]^{-1/2} \quad (5.8)$$

where v_0 is the initial velocity, v_p is the final velocity, c is the speed of light, m is the mass of the projectile's distance traveled, and F_i the constant ionization rate. The equation proves that the velocity of the projectile is directly proportional to the mass and distance traveled. Consequently, the projectile will have little potential to ionize and explore when the distance is long and the mass is small. Therefore, bigger projectiles are those transversing shorter distances and exhibit vast ionization potentials and exploration capabilities.

To improve the algorithm's exploration capabilities, the concept of "forking" is designed. Projectile emits two symmetrical channels similar to the phenomenon of lightning forking. In this algorithm, forking is defined in two ways. Equation 5.9 presents the mathematical expression of the symmetrical channels that define nuclei collision which leads to the creation of symmetrical channels.

$$\vec{p}_i = x + y - p_i \quad (5.9)$$

where \vec{p}_i and p_i are the opposite and original projectiles, and x and y are the boundary limits in one dimension. This mechanism aims to improve the quality of less successful solutions within the population. Otherwise, one of the channels at the forking tip emerges to balance the c . Equation 5.10 demonstrates that the shaping parameter (α) exert a significant influence over the trajectory. In the lightning search algorithm, the value of α for a specific space projectile p^s is dynamically determined by its distance from the current lead projectile P^l . This distance-dependent relationship directly influences the movement of the space projectile, as expressed;

$$p_{i_{new}}^s = p_i^s \pm \text{exprand}(\alpha_i) \quad (5.10)$$

If the calculated new position P_{new}^S of the space projectile is negative, it indicates a movement in the opposite direction. However, simply moving in the opposite direction doesn't guarantee successful channel formation. For successful propagation, the space projectile's energy $E_{p_i}^S$ must exceed the energy of the existing step leader E_i^{sl} . Only then can the space projectile extend the existing channel. If the new position $P_{i_{new}}^S$ leads to a successful channel extension, the corresponding step leader s_i^l is extended to this new position, and the space projectile's position is updated accordingly. Otherwise, both the space projectile and the step leader remain in their previous positions. If a particular space projectile successfully extends the step leader beyond the current longest leader in the system, it is then designated as the new lead projectile.

5.3.1.1 Lead Projectile

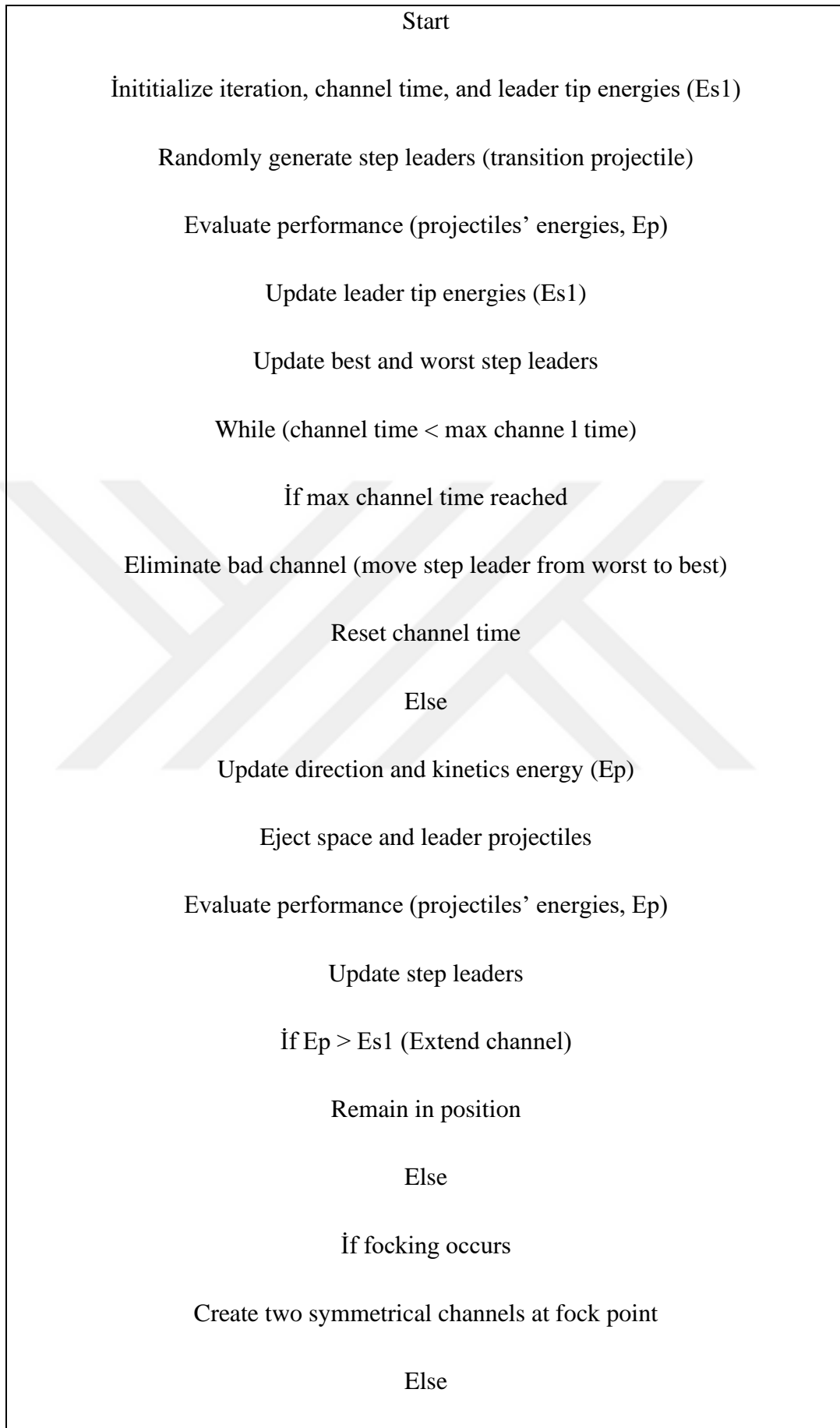
Following [30], Analogous to the generation of space projectiles, the position of the lead projectile can be updated probabilistically. This update incorporates a random component generated from a normal distribution. The probability density function (PDF of the normal distribution can be expressed as:

$$f(x^l) = \frac{1}{\sigma\sqrt{n\pi}} e^{-\frac{(x^l-\alpha)^2}{2\sigma^2}} \quad (5.11)$$

equation 5.11, demonstrates that the shaping parameter (α) significantly influences the directional exploration of the space projectile. In the LSA context, the parameter α^i for a specific space projectile P_i^S is dynamically determined by its proximity to the current lead projectile. This distance-dependent parameter governs the search behavior of the space projectile, influencing its movement within the solution space. The position of the space projectile P_i^S as shown in equation 5.12 at the subsequent step can be mathematically expressed as

$$P_{i_{new}}^L = p_i^l \pm \text{normrand}(\mu_L, \sigma_L) \quad (5.12)$$

Figure 5.4 contained the pseudocode for writing the code for the simulation of LSA technique.



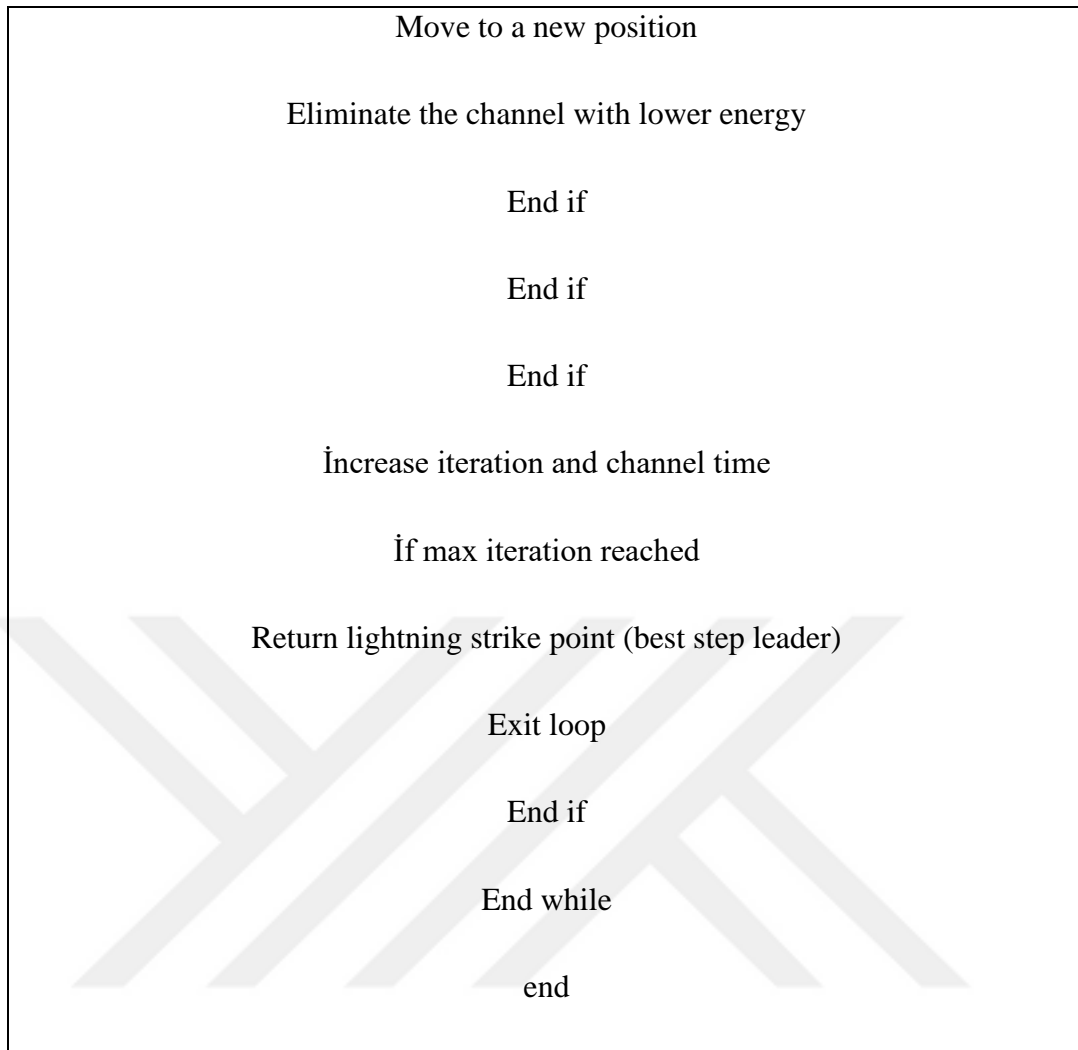


Figure 5.4. Pseudocode of the LSA.[30]

5.4 Artificial Rabbit Optimization

Artificial Rabbit Optimization (ARO) is a recently developed metaheuristic algorithm introduced in 2022. It draws inspiration from the foraging and hiding behaviour of a real rabbit, incorporating their energy dynamics that facilitate transitions between these strategies. The corresponding mathematical models are presented, and ARO proves to be an efficient and reliable approach for solving complex optimization problems, as demonstrated in this study. Figure 5.5 presents a rabbit net with some burrows.



Figure 5.5. A rabbit net with several burrows [31]

5.4.1 Exploration

As described earlier, rabbits prioritize distant areas and disregard nearby resources during the foraging, consuming grass randomly in other regions rather than their own. This behavior, termed “detour foraging,” is emulated in the Artificial Rabbit Optimization (ARO) algorithm. Each rabbit in the swarm is assumed to occupy its region containing grass and d burrows, while also visiting the positions of the other rabbits randomly for foraging. In practice, rabbits tend to explore around a food source to secure sufficient sustenance. Consequently, the detour foraging behavior in ARO reflects the tendency of each search agent to update its position toward a randomly selected individual within the swarm, incorporating a perturbation for variability [31]. The mathematical model representing this behavior is as follows:

$$\begin{aligned} \vec{V}_i(t+1) &= \vec{x}_j(t) + R \cdot (\vec{x}_i(t) - \vec{x}_j(t)) + \text{round}(0.5 \cdot (0.05 + r_1)) \cdot n_{1,i,j} \\ &= 1, \dots, n \text{ and } j \\ &\neq i \end{aligned} \quad (5.13)$$

$$R = L \cdot c \quad (5.14)$$

$$L = \left(e - e^{\left(\frac{t-1}{T}\right)^2} \right) \cdot \sin 2\pi r_2 \quad (5.15)$$

$$c(k) = \begin{cases} 1, & \text{if } k == g(l) \\ 0, & \text{else} \end{cases} \quad k = 1, \dots, d \text{ and } l = 1, \dots, [r_3 \cdot d] \quad (5.16)$$

$$g = \text{randperm}(d) \quad (5.17)$$

$$n_1 \sim N(0,1) \quad (5.18)$$

where $\vec{V}_i(t+1)$ is the candidate position of the i^{th} rabbit at the time $t+1$, while $\vec{x}_j(t)$ represents its position at iteration t . n represents the total number of the rabbit population, d corresponds to the dimension of the problem. T is the maximum number of the iteration, $[\cdot]$ is the ceiling function, round indicates rounding to the nearest integer, randperm returns a random permutation of the integers from 1 to d . Additionally, $r_1, r_2, \text{ and } r_3$ are three random numbers in the range of $(0,1)$. The parameter L denotes the running length, which quantifies the step size when performing the detour foraging, and n_1 follows a standard normal distribution.

In equation 5.13, the perturbation may assist ARO to avoid local extrema and perform a global search. And equation 5.15, the running length L , can generate a longer step during the initial iterations. It selects one of the burrows for hiding to decrease the probability of being attacked [32].

5.4.2 Exploitation (Random Hiding)

Following [32], to escape from predators, a rabbit typically digs multiple burrows around its nest as potential hiding spots. In this algorithm, at each iteration, a rabbit always constructs d burrows along each dimension of the search space. The j^{th} burrow of the i^{th} rabbit is generated by.

$$\vec{b}_{i,j} = \vec{x}_i(t) + H \cdot g \cdot \vec{x}_i(t), i = 1, \dots, n \text{ and } j = 1, \dots, d \quad (5.19)$$

$$H = \frac{T - t + 1}{T} \cdot r_4 \quad (5.20)$$

$$n_2 \sim N(0,1) \quad (5.21)$$

$$g(k) = \begin{cases} 1, & \text{if } k == j \\ 0, & \text{else} \end{cases} \quad k = 1, \dots, d \quad (5.22)$$

According to eq. (5.19), the d burrows are generated within the proximity of a rabbit along each dimension. H is the hiding parameter which decreases linearly from 1 to $1/T$ over the course of iteration, incorporating a random perturbation. Initially, these burrows are generated in a bigger neighbourhood around the rabbit. However, as the iterations rise, this neighbourhood shrinks too.

In the wildlife of a rabbit, a chase is a norm. so to survive, the rabbit needs a hiding place. As a result, they are inclined to stochastically select a burrow from their burrows for sheltering to avoid getting caught. The hiding strategy can be formulated mathematically from equation 5.23-5.25.

$$\vec{v}_i(t+1) = \vec{x}_i(t) + R \cdot (r_4 \cdot \vec{b}_{i,r}(t) - \vec{x}_i(t)), i = 1, \dots, n \quad (5.23)$$

$$g_r(k) = \begin{cases} 1, & \text{if } k == [r_5 \cdot d] \\ 0, & \text{else} \end{cases} \quad k = 1, \dots, d \quad (5.24)$$

$$\begin{aligned} &\vec{b}_{i,r}(t) \\ &= \vec{x}_i(t) + H \cdot g_r \cdot \vec{x}_i(t) \end{aligned} \quad (5.25)$$

Here, $\vec{b}_{i,r}$ denotes a randomly selected burrow for hiding among the d available burrows, and r_4 and r_5 are two random numbers in $(0,1)$. Based on eq. (5.23), the i^{th} Search individual attempts to update its position toward the selected burrow.

After one of both detour foraging and random hiding is achieved, i^{th} rabbit will be updated as follows:

$$\vec{x}_i(t+1) = \begin{cases} \vec{x}_i(t), & f(\vec{x}_i(t)) \leq f(\vec{v}_i(t+1)) \\ \vec{v}_i(t+1), & f(\vec{x}_i(t)) > f(\vec{v}_i(t+1)) \end{cases} \quad (5.26)$$

5.4.3 Energy Shrink (switch from exploration to exploitation)

Following [33], In ARO, at the initial phase, rabbits often conduct detour foraging while frequently performing random hiding in the later phase of iteration. The energy of the rabbit is what drives the mechanism but it shrinks over the course of the iterations. Therefore, the energy factor in ARO is formulated as follows:

$$A(t) = 4 \left(1 - \frac{t}{T}\right) \ln \frac{1}{r} \quad (5.27)$$

An energy factor is calculated to regulate the transition from exploration to exploitation in ARO. Where r represents a random variable. In ARO, when the energy factor $A(t) > 1$, the rabbit tends to search different foraging spaces randomly within the phase of the exploration. The pseudocode of ARO is given in Figure 5.6

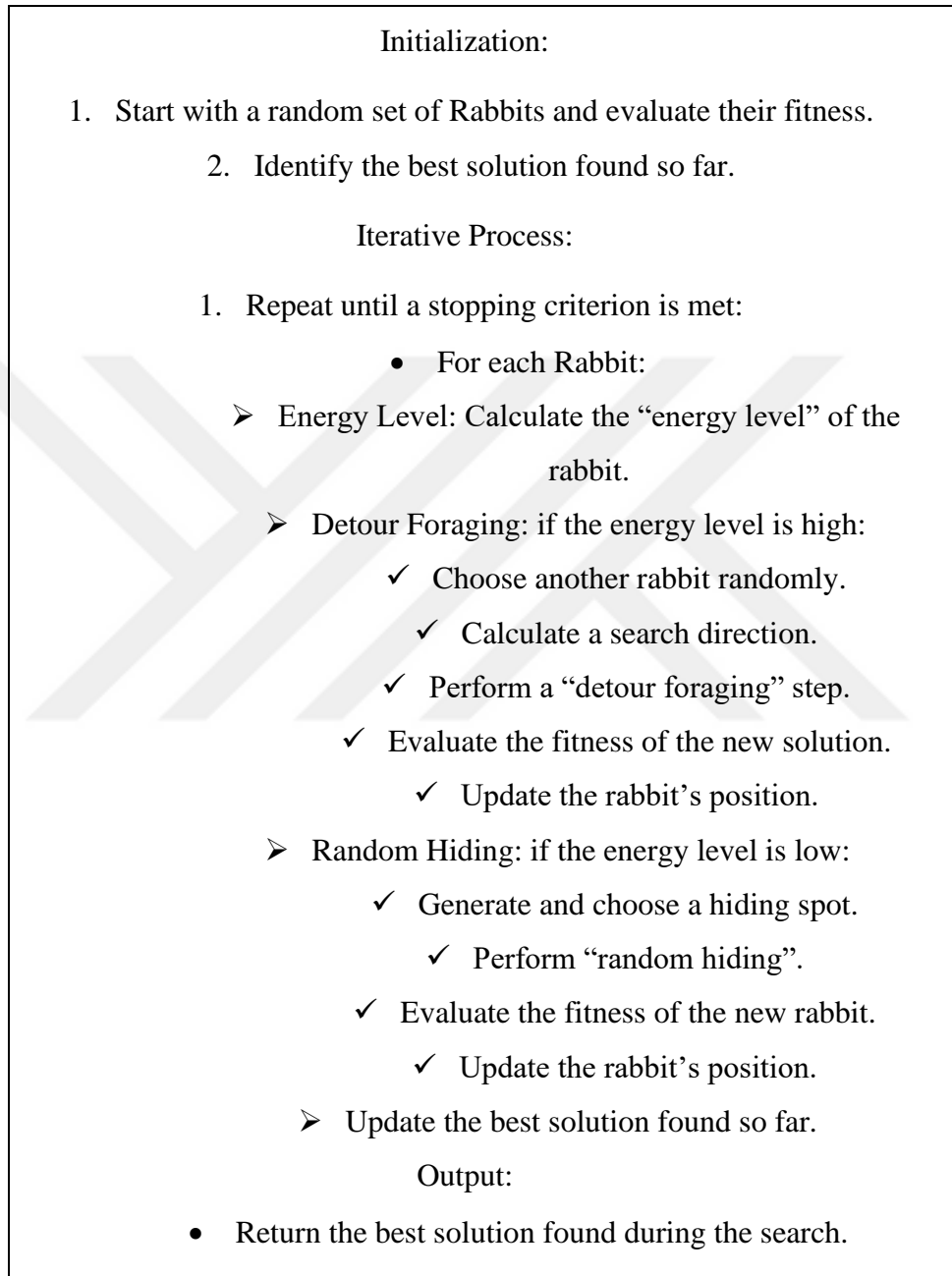


Figure 5.6. General steps to apply ARO [33]

5.5 Conclusion

In this study, we explored the fundamental principles and mathematical formulations of several nature-inspired metaheuristic algorithms, including the WOA, LSA, and

ARO. Each of these algorithms is designed to mimic natural behaviors observed in different species and physical phenomena to enhance optimization performance.

WOA is inspired by the hunting strategies of humpback whales, employing techniques such as encircling prey, bubble-net attacking, and random exploration to balance global and local search capabilities. LSA, modeled after the phenomenon of lightning, leverages projectile motion and ionization-based propagation to enhance solution space exploration. Meanwhile, ARO emulates the foraging and hiding behaviors of rabbits, incorporating detour foraging and random hiding mechanisms to ensure a robust search process. By leveraging the unique characteristics of these algorithms, this study demonstrates how bio-inspired and physics-based optimization techniques can be applied to complex problems, particularly in PID parameters tuning.

CHAPTER 6

SIMULATION RESULT AND DISCUSSION

6.1 Introduction

In this chapter, extensive studies were conducted under different scenarios aiming to explore the performance of the single-area and two-area power systems. The study is arranged on a case-by-case basis, from simple to more complicated, introducing and integrating renewable energy with constant and variable inputs, as well as optimizing the PID parameters with metaheuristic optimization techniques employed. Furthermore, the evaluation of energy storage systems is followed by an assessment of their impact on enhancing the stability of the power systems.

6.1.1 Case 1

In this case study, the single-area system is operated with conventional PID parameters with values (8.6147,10, 4.1436) without any RES or ESS integration. This system is simulated under a perturbation of step load change of 0.2 pu applied at 0 seconds. The comparison of the system's change in frequency with and without the PID controller is shown in Figure 6.1. It is noted that the system frequency has a steady-state value of -0.0096 P.U. at 9.6 seconds when the PID controller is not activated. With the proper tuning of the PID controller, zero steady-state error in frequency change is attained at 12 seconds. Figure 6.2, shows that the system's power output is stabilized at 0.2 P.U. in a duration of around 8.3 seconds, which is equivalent to the load demand. Without a PID controller, it is observed that the system's power output remains below the load demand.

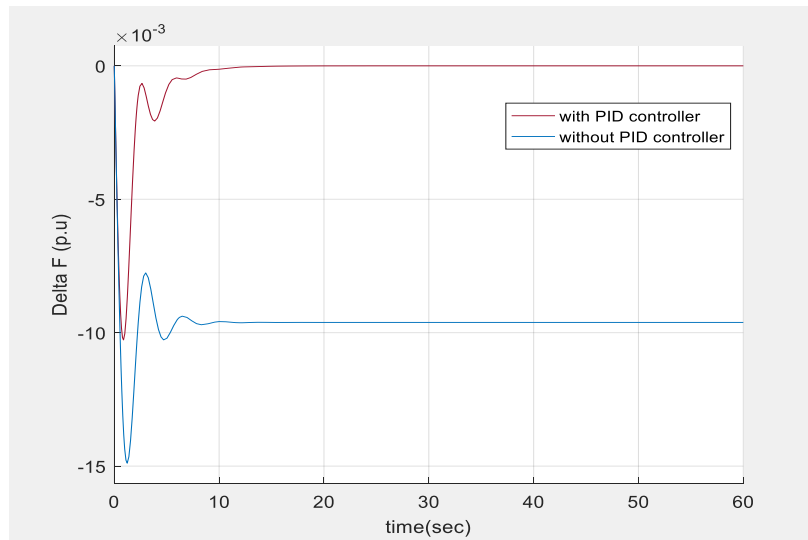


Figure 6.1. Comparison of the system's change in frequency with and without PID controller

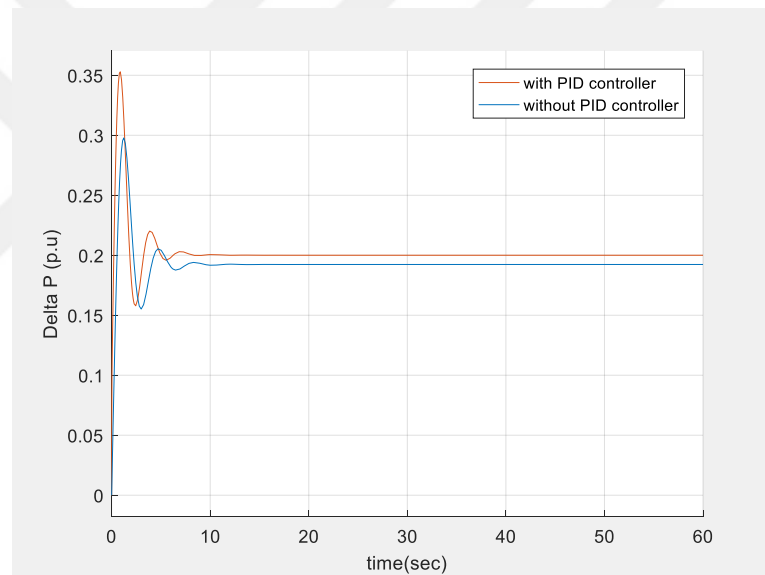


Figure 6.2. Comparison of the power output of the system with and without PID controller

6.1.2 Case 2

In this case study, PV and WT systems are added to the single-area system as shown in Figure 6.3. The system is exposed to severe load and irradiation variations as shown in Figure 6.4. At 2 s, the load increases from 0 to 0.1 p.u. then at 10 s, it drops to -0.05 p.u. The PID controller parameters are optimized using the aforementioned optimization methods (ARO, LSA, and WOA) which are simulated for 100 iterations, with 0 as the lower boundary and 10 as the upper boundary. For all, the population size is set as 50. The optimization results are presented in Table

6.1 shows the optimization results when only the WT system is enabled. The optimization methods give the lowest settling time of 22.7 s for WT. On the other hand, Figure 6.5 compares three optimization methods for PID parameter tuning under constant WT and variable load. In this figure 6.5, at 2s, the system experiences a big overshoot and the subsequent drop and a small overshoot at 10 s. ARO tuned PID controller causes fewer oscillations, the least settling time, and the smallest overshoot.

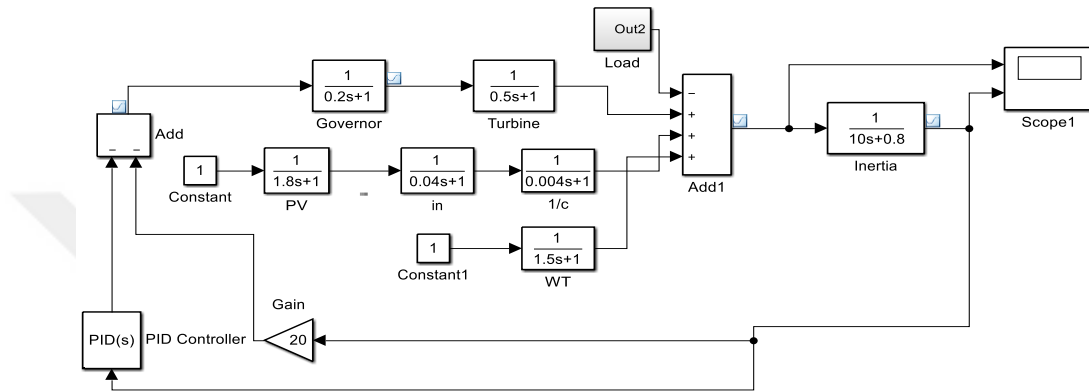


Figure 6.3. Transfer function representation of the single-area system with PV and WT integration

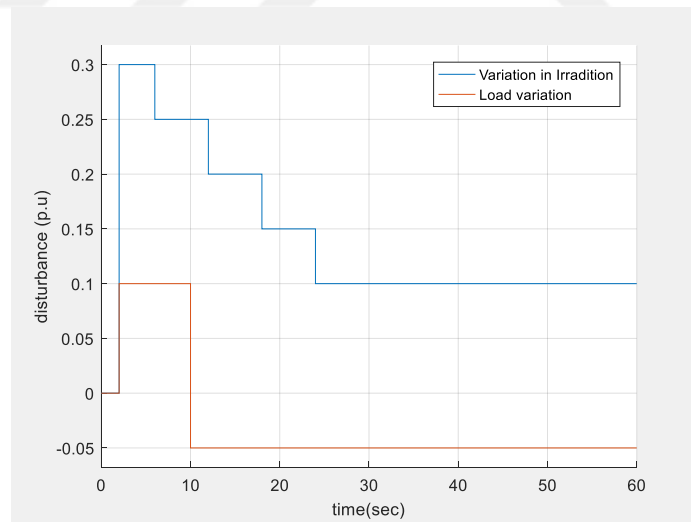


Figure 6.4. The disturbances used as input to the system

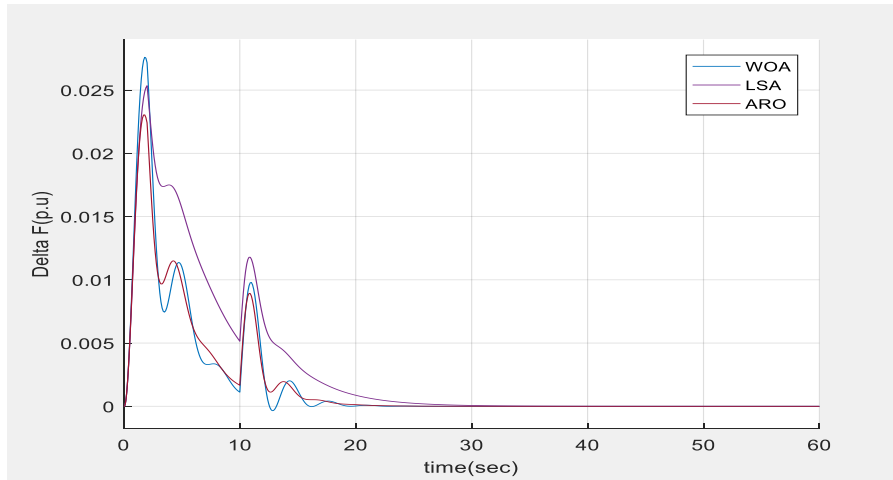


Figure 6.5. Comparison of ARO, LSA, and WOA under constant WT and variable load

Table 6.1. Optimization results for PID parameters for single-area system under constant wind speed

Optimization method	ITAE	overshoot	undershoot	Settling time	PID parameters (K, K_i, and K_d)
ARO	0.5174	0.025	0	22.7	8.8427, 10, 4.3477
WOA	3.21	0.0301	0	60	7.5469, 3.3712 2.3995
LSA	0.5147	0.0312	0	23.2	4.3118, 9.4766 1.8173

6.1.3 Case 3

The performance of the three optimization algorithms ARO, WOA, and LSA has been evaluated for a single-area power system integrated with constant PV and WT. The simulation results, shown in Table 6.2, highlighted the effectiveness of each optimization method in enhancing the system's stability by minimizing frequency deviations caused by load disturbances. ARO achieved the lowest ITAE value of 0.5985, indicating superior performance in reducing the overall system error. Undershoot and overshoot are critical in evaluating system stability, as they indicate how much the system deviates from the desired steady-state frequency. While WOA has the lowest undershoot, the balance between undershoot and overshoot makes

ARO more favorable in terms of overall stability. The proportional and integral gains are higher in ARO which contributes to faster system stability, while the derivative is tuned to reduce oscillations. Figure 6.6 shows the ARO curve with minimal oscillations and achieves steady-state frequency faster than the other two.

Table 6.2. Optimization results for PID parameters for single-area system under constant irradiation and constant wind speed

Optimization method	ITAE	Undershoot $\times 10^{-3}$	Overshoot $\times 10^{-3}$	Settling time	PID parameters (K , K_i , and K_d)
ARO	0.5985	0.454	4.944	15.12	10, 10, 3.0713
WOA	0.9747	0.026	4.59	17.1	9.4301, 6.5550, 6.2250
LSA	4.285	7.5	2.61	39.1	3.1908, 5.9219, 7.7052

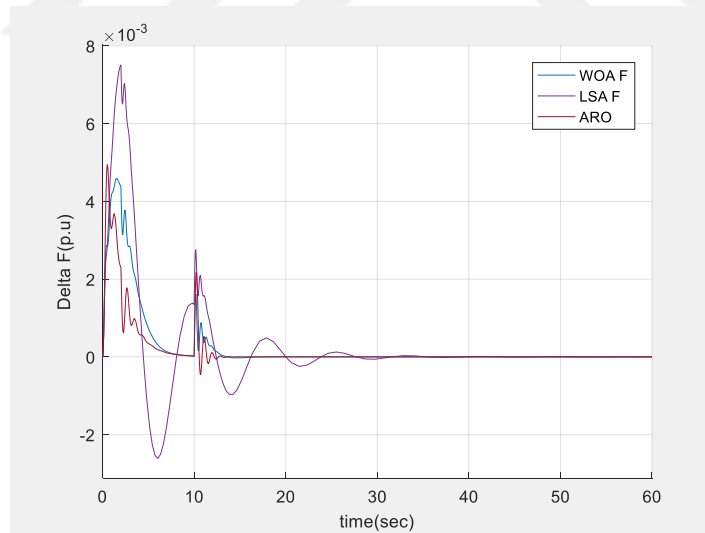


Figure 6.6. Comparison of ARO, WOA, and LSA under constant RES in a single–area system

6.1.4 Case 4

The wind turbine is considered to have an input of white noise generating random numbers. This is closer to reality since the wind blows continuously and is unstable as shown in Figure 6.7. The solar irradiation is increased to 0.3 p.u at 2 s according

to Figure 6.4, and then began to decrease by -0.05 p.u step by step at 6, 12, 18, and 24 s until it is reduced to 0.1 p.u as in case 3. Figure 6.8, shows the frequency response of the system, and all optimization methods respond well, especially ARO as it shows better damping of oscillations compared to WOA and LSA, indicating faster adaptation to random noise and solar variations, and better frequency stability during the stepwise decrease in solar irradiation. LSA struggles to handle the noise effectively, leading to large and more persistent oscillation. WOA performs moderately well but shows slightly higher oscillation.

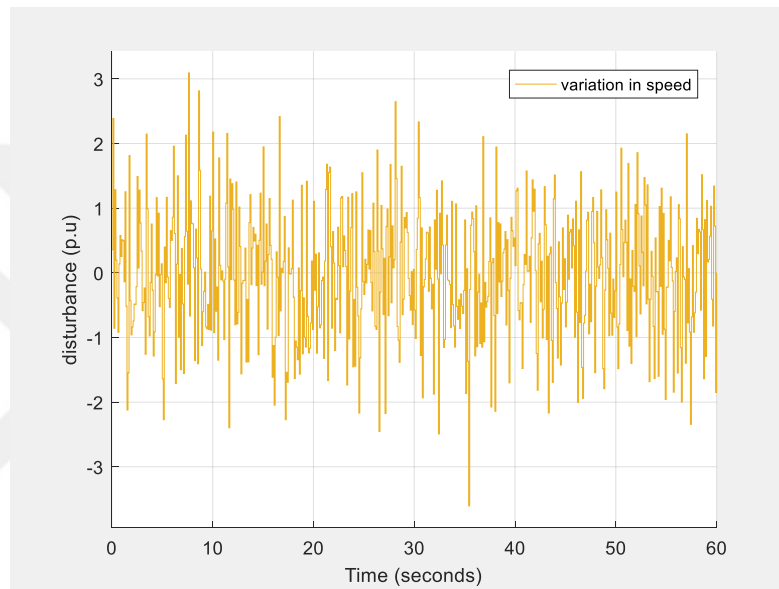


Figure 6.7. White noise is used as a variation in the speed of WT

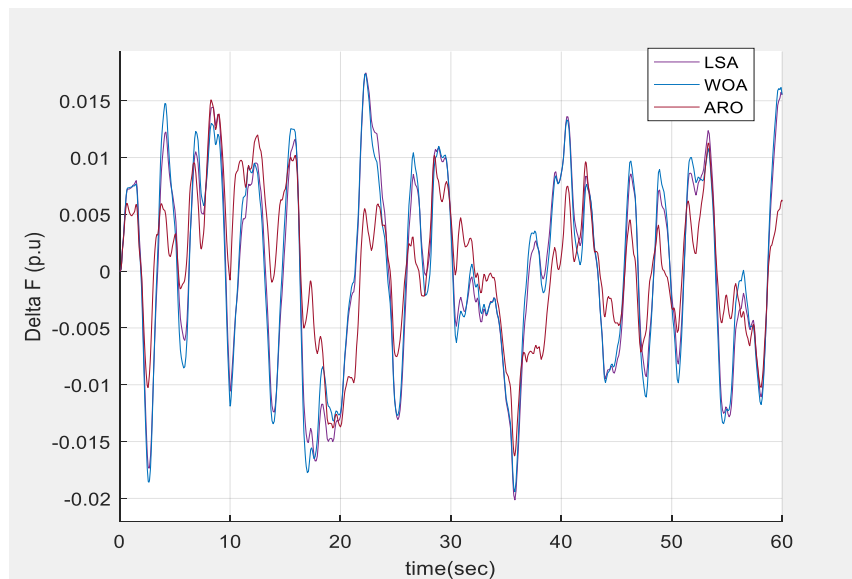


Figure 6.8. Comparison of ARO, LSA, and WOA under severe disturbances

6.1.5 Case 5

The two-area power system is simulated using the parameters listed in Table 6.3 in the following case studies. Several simulation scenarios are rendered to thoroughly investigate the system stability with respect to steady-state frequency and power output. The optimization performance of the aforementioned optimization methods on PID controller parameter tuning is also investigated. Different types of ESSs are employed in the system to play a stability control role. A load disturbance of 2% is applied in Area-1 and 1.5% in Area-2, each at 2 s. Figure 6.9 illustrates the steady-state frequency of the system in both areas. Long undershoots and short overshoots right at 2 s are observed, then the system reaches a steady-state condition at 21.8 s as indicated in Table 6.4. These results show the effectiveness of the LFC under an area control error strategy in which each load demand is compensated by the governor assigned to that area. On the other hand, Figure 6.10 shows the output power of the two-area system and the two overshoots at 2 s confirm the surge in the load in both areas. The subsequent steady-state at zero shows the system stability and effectiveness of the automatic LFC approach.

Table 6.3. Parameters of the two-area systems

Parameter Name	Area-1	Area-2
Speed Regulation (R)	0.05	0.0625
Frequency Load Coefficient (D)	0.6	0.9
Inertia constant (H)	5	4
Base power(s)	1000MVA	1000MVA
Governor Time Constant (T_g)	0.2	0.3
Turbine Constant (T_t)	0.5	0.6
Integrator gain (K_i)	0.3	0.3
Nominal frequency	60Hz	60Hz

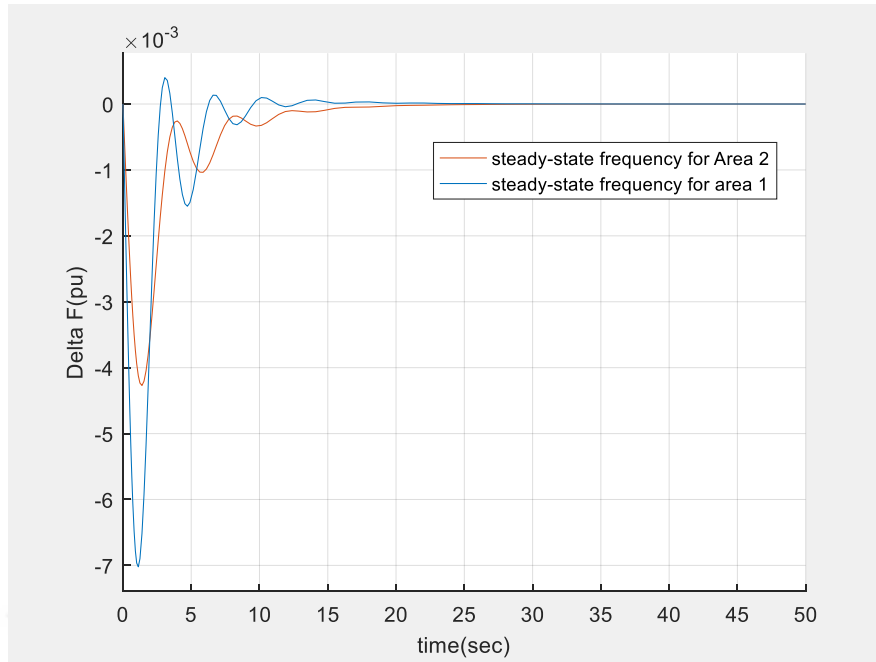


Figure 6.9. Frequency deviation of the system tested under different load surges in Areas 1-2

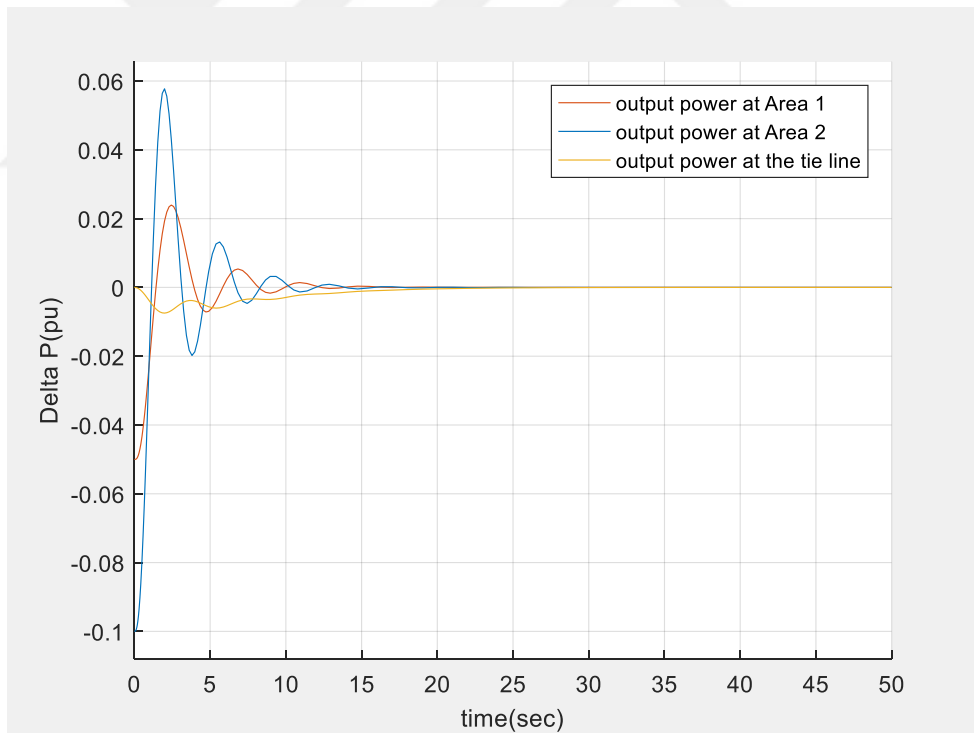


Figure 6.10. The power output produced by the two areas and the tie line

Table 6.4. Comparison of ESS performances on the two-area system

ESS type	Overshoot $\times 10^{-3}$		Undershoot $\times 10^{-3}$		Settling time (s)	
	Area-1	Area-2	Area-1	Area-2	Area-1	Area-2
No ESS	2.8	1.9	-14.6	-14.9	21.8	28.1
FESS	0	0	-8.3	-6.85	32.4	43.1
SMESS	0	-3	-10.1	-8.7	29.8	35.6
BESS	0	0	-8.8	-7.22	35.5	43.5

To further enhance the system's stability and steady-state frequency, ESSs are tested to investigate their effects. Figures 6.11 and 6.12 present the steady-state frequency due to each ESS. Table 6.5 offers the performance indices, where the FESS has the shortest undershoot in both areas followed by BESS and then SMESS. The overshoots seem to die out except for SMESS, and the settling time is a disadvantage for all the ESSs. Figures 6.13 and 6.14 show the steady-state power output of both areas in response to the step load perturbation of 0.2 p.u for Area-1 delivered at 2 s and 0.15 p.u for Area-2 at 2 s. FESS shows a significant improvement in the overshoots of the system followed by BESS, SMESS as reported in Table 6.5. However, the settling time is seen to be disadvantageous for the ESSs in both areas. In a nutshell, ESSs are seen to dampen the oscillations and increase the settling time. Figure 6.15 represents the tie-line steady-state power output due to the ESSs.

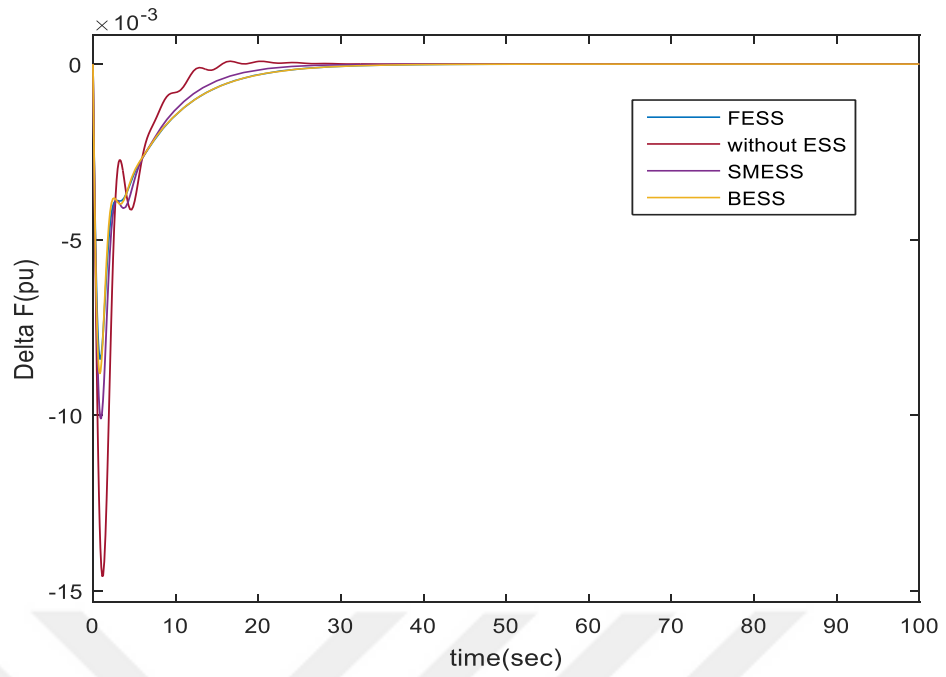


Figure 6.11. Comparison of the frequency deviation in Area-1 due to the ESS

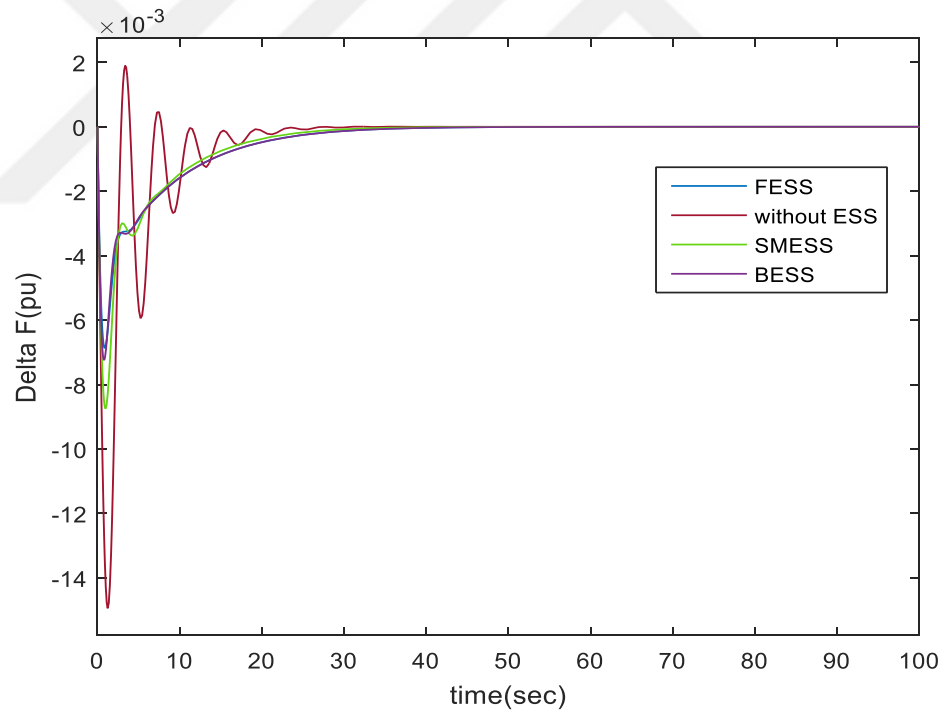


Figure 6.12. Comparison of frequency deviation in Area-2 due to ESS

Table 6.5. Comparison of power output parameters due to ESS

ESS type	Overshoot $\times 10^{-3}$		Undershoot $\times 10^{-3}$		Settling time (s)	
	Area-1	Area-2	Area-1	Area-2	Area-1	Area-2
No ESS	182	125	136	110	43.1	28.1
FESS	327	281	158	86	27.1	28.1
SMESS	220	159	148	120	35.6	28.1
BESS	187	127	132	107	43.1	28.1

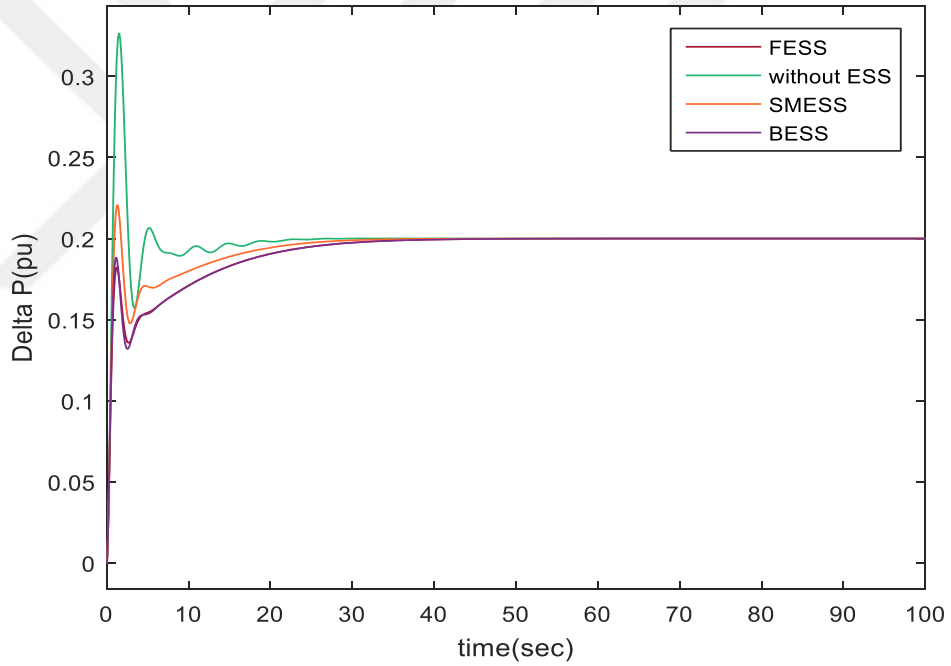


Figure 6.13. The power output due to ESS at Area-1

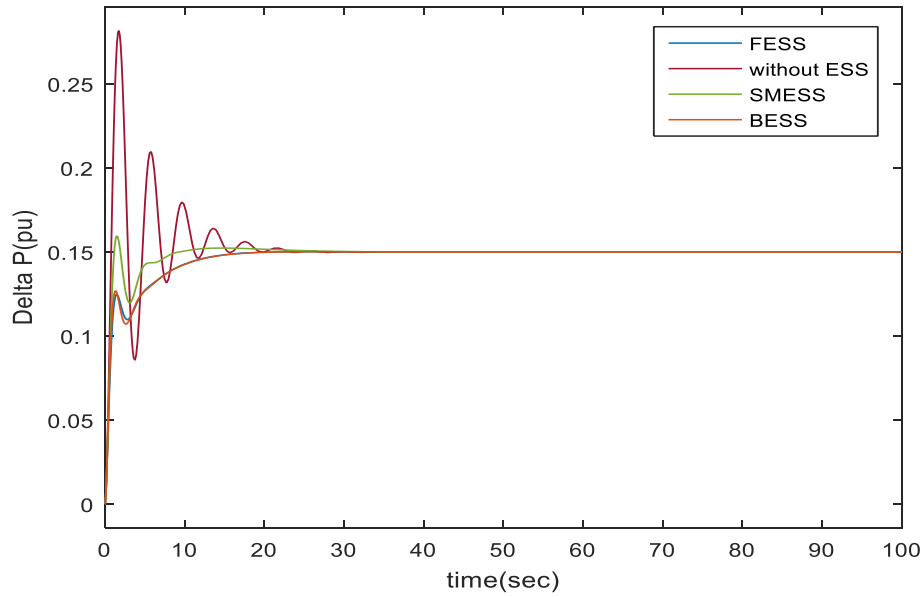


Figure 6.14. The power output due to ESS in Area-2

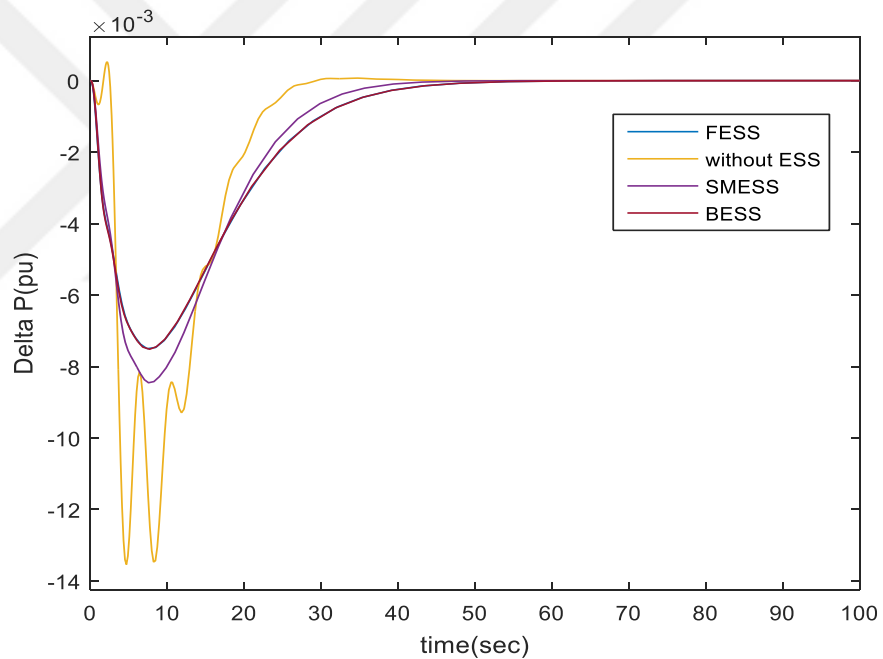


Figure 6.15. The tie-line steady-state power output due to the ESSs

6.1.6 Case 6

RES such as PV and WT systems are activated in the two-area system. Figure 6.16 shows the model configuration. This study is evaluated based on the optimization techniques and the indices upon which the selection of the best technique depends is the popular error criteria, namely “ITAE” and then the overshoot, undershoot as well as the settling time. The system responds to the significant load perturbation as illustrated in case 3. The overshoot at the corresponding times can be observed in

Figures 6.17 and 6.18, representing Area-1 and 2. The ARO is seen to have a minimum ITAE of 0.2126 in Area-1 and 0.6035 in Area-2 compared to WOA and LSA as can be seen in Table 6.6. The ARO has also the least overshoot and undershoot in both areas. These results prove the superiority of ARO method on the overall basis compared to the LSA and WOA methods.

Table 6.6. Comparison of optimized parameters for the two-area system under constant RES

Optimization Method	ITAE1	ITAE2	Overshoot× 10 ⁻³		Undershoot× 10 ⁻³		Settling time (s)	
			Area-1	Area-2	Area-1	Area-2	Area-1	Area-2
LSA	0.4809	27.04	3.9	2.97	0	0	100	100
WOA	0.406	0.2221	8.1	3.93	-1.2	-0.24	16.9	26.4
ARO	0.2126	0.6035	2.4	2.22	-0.8	-0.42	29.8	21.4

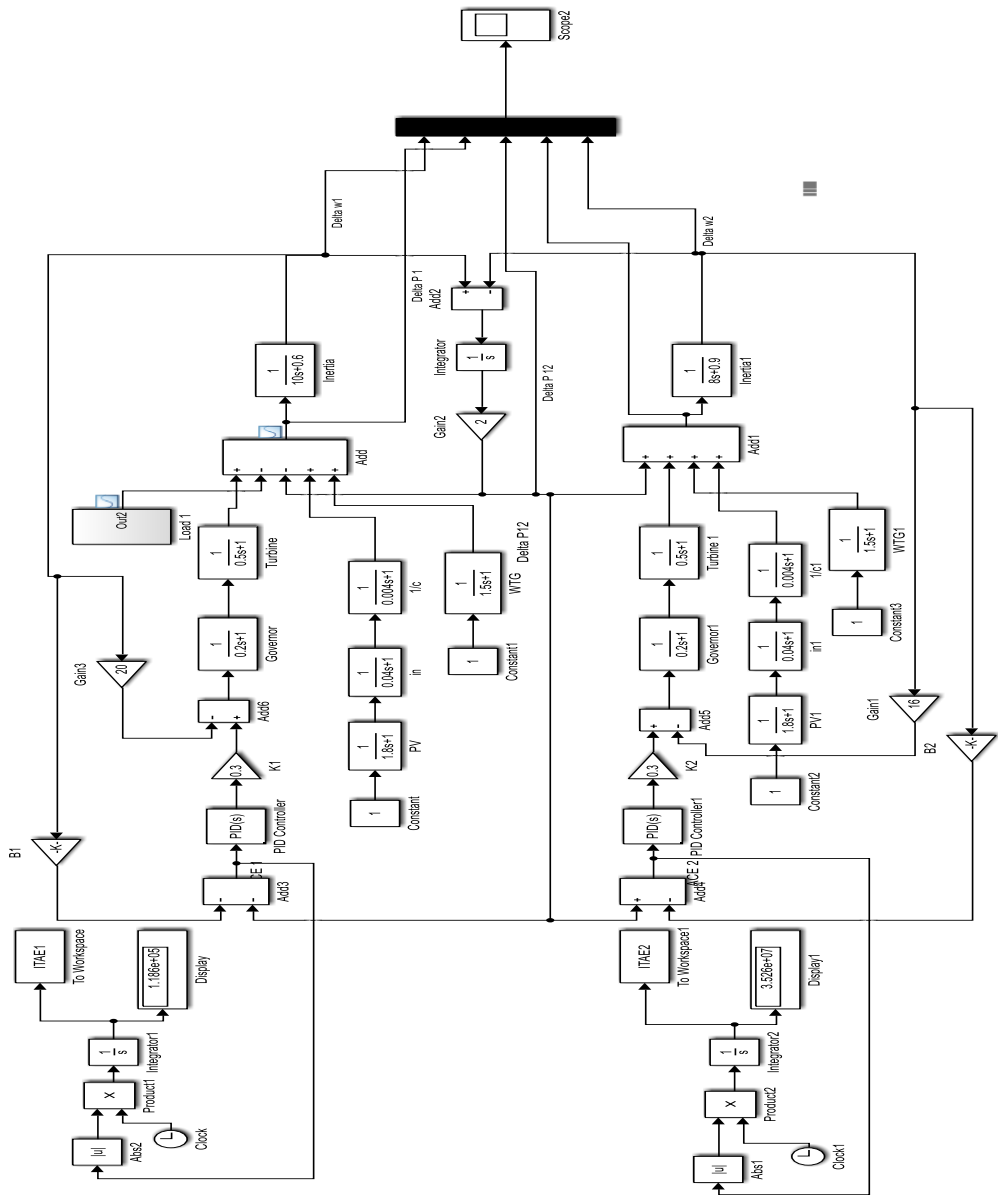


Figure 6.16. Renewable energy penetration with a constant input in both areas

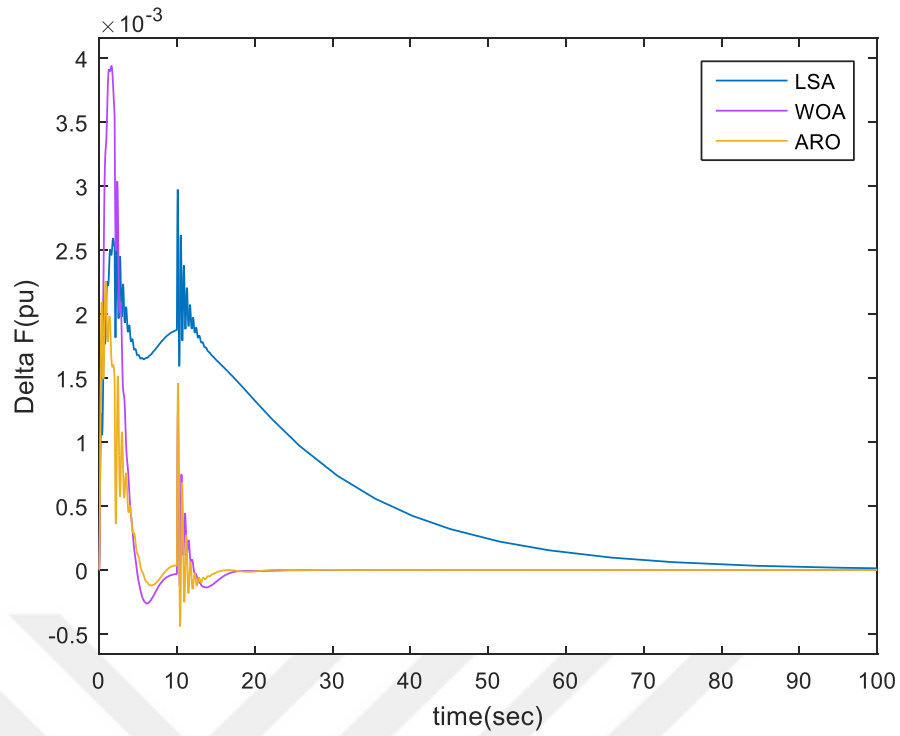


Figure 6.17. The frequency deviation of Area-1 under constant PV, WT, and variable load

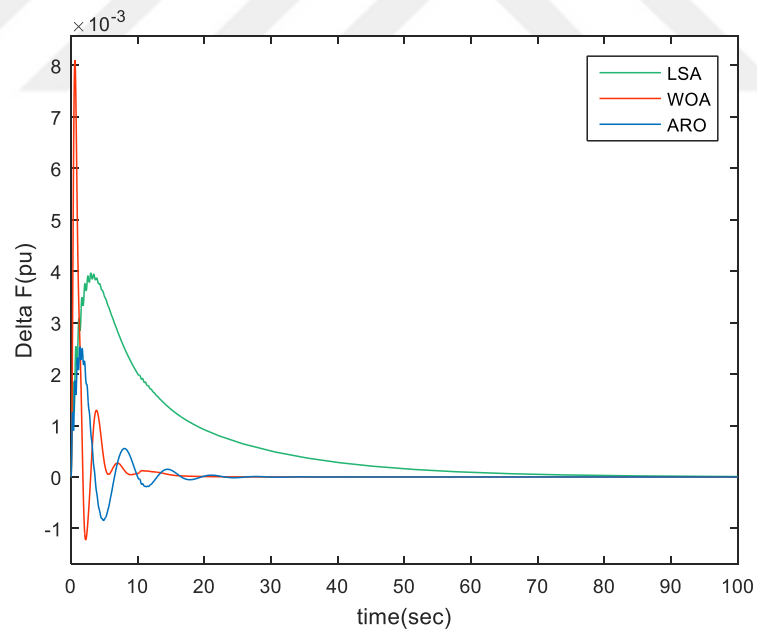


Figure 6.18. Comparison of frequency deviation of Area-2 under constant PV, WT, and no load

6.1.7 Case 7

The configuration of the overall system constituting PV, WT, and the load is shown in Figure 6.19. The main aim of this case is to examine the superiority of ARO in

subduing a complex disturbance in the system due to the severe disturbances from the PV, WT, and the load as illustrated in Figure 6.20. The load surges at 2 s to 0.1 p.u and then drops to -0.05 p.u at 10 s. This fluctuation is reflected at the corresponding time in Figure 6.20 since the load is only applied to Area-1. Both PV and WT systems have a steady increment in disturbance of 0.05 p.u at 0,7,11,16 and 20 s. The only difference is that there is an abrupt fall of WT speed at 20 s to -0.05 p.u. Under these disturbances. The optimization techniques are applied to improve the PID controller parameters. Table 6.7 provides the quantitative analyses of Figures 6.21 and 6.22 which represent Area-1&2. The ARO method has the lowest ITAE of 0.3431 for Area-1 and 0.2642 for Area-2, providing a minimum settling time of 33.1 s.

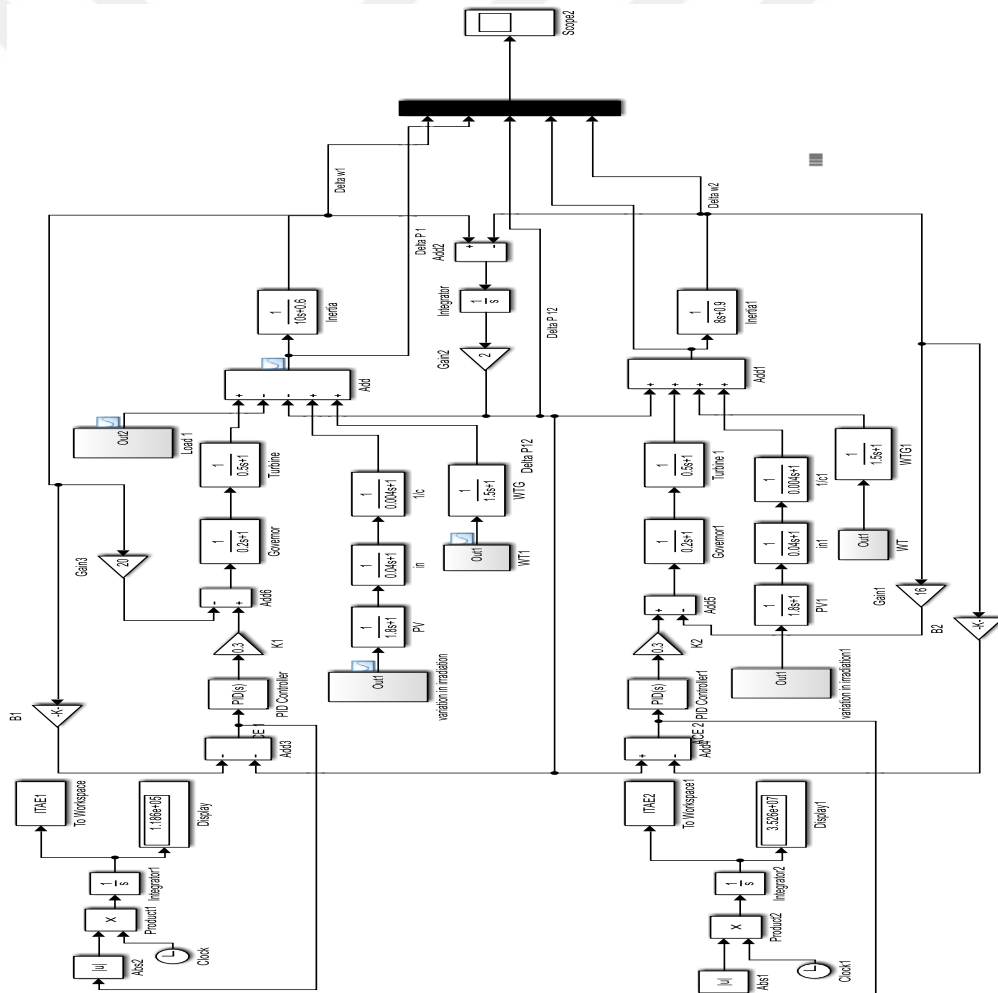


Figure 6.19. Integration of RES into the System model in both areas and Load disturbance in Area-1

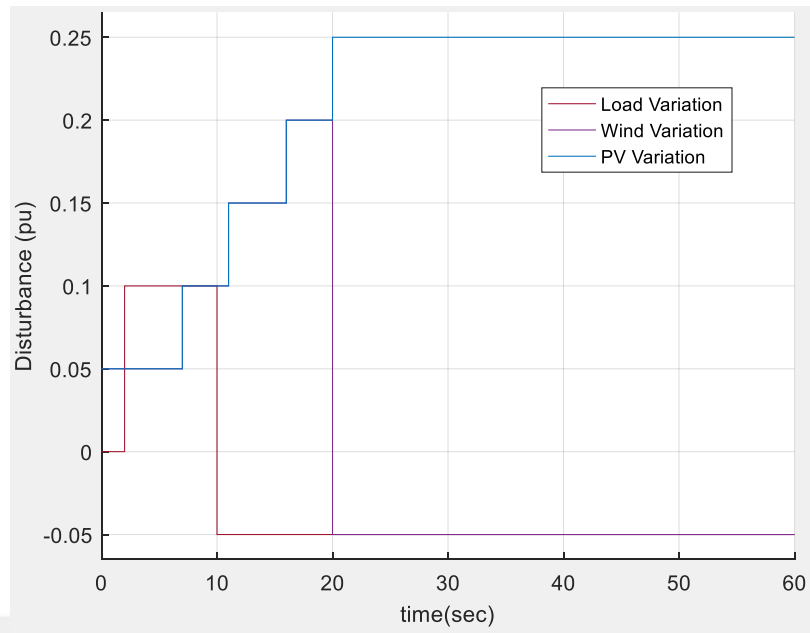


Figure 6.20. The disturbances applied to the system

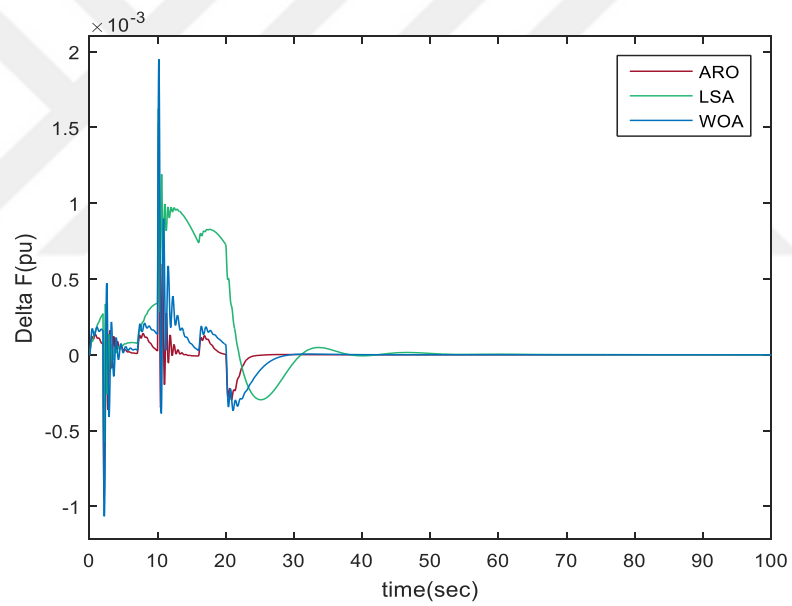


Figure 6.21. Comparison of frequency deviation optimizations in Area-1

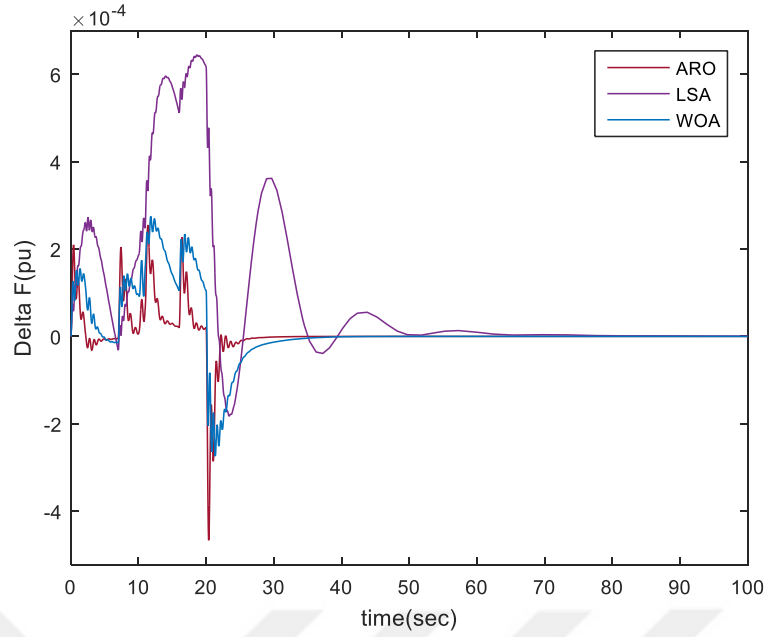


Figure 6.22. Comparison of frequency deviation optimizations in Area-2

Table 6.7. Parameters due to optimizations under variable load and ESS in both areas

Optimization Method	ITAE1	ITAE2	Undershoot× 10 ⁻⁴		Overshoot× 10 ⁻⁴		Settling time (s)	
			Area-1	Area-2	Area-1	Area-2	Area-1	Area-2
WOA	0.9458	0.5858	-10.3	-2.74	19.5	2.75	30.1	43.7
LSA	3.943	2.386	-5.6	-1.8	16.2	6.43	51.8	100
ARO	0.3431	0.2642	-9.5	-4.67	15.3	2.55	25	33.1

6.1.8 Case 8

Under constant PV, WT, and variable load, the two-area system is tested by charging and discharging FESS. The responses are presented in Figures 6.23, 6.24, and 6.25. Furthermore, under variable load and RES conditions, the responses are illustrated in Figures 6.26, 6.27, and 6.28. Numerous research papers explore the technology of charging and discharging ESS. On the other hand, FESS can be preferred due to its fast response and durability [34]. The smoother response of FESS in the charging

phase can be compared to the discharging state. Both charging and discharging states are effective but the intrinsic characteristics of charging tend to result in smoother damping of oscillations [35][36].

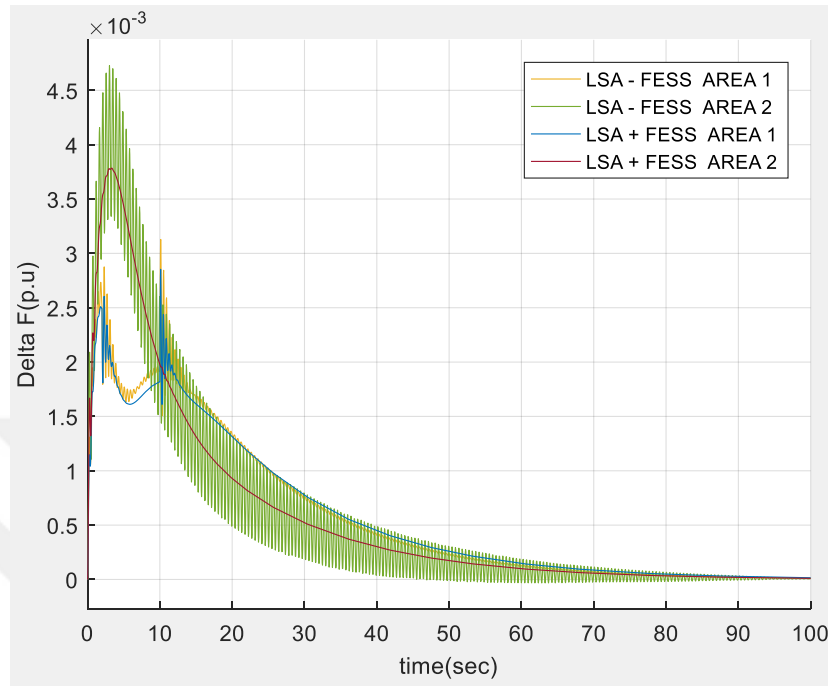


Figure 6.23. Frequency deviation comparison under LSA on charging and discharging of FESS.

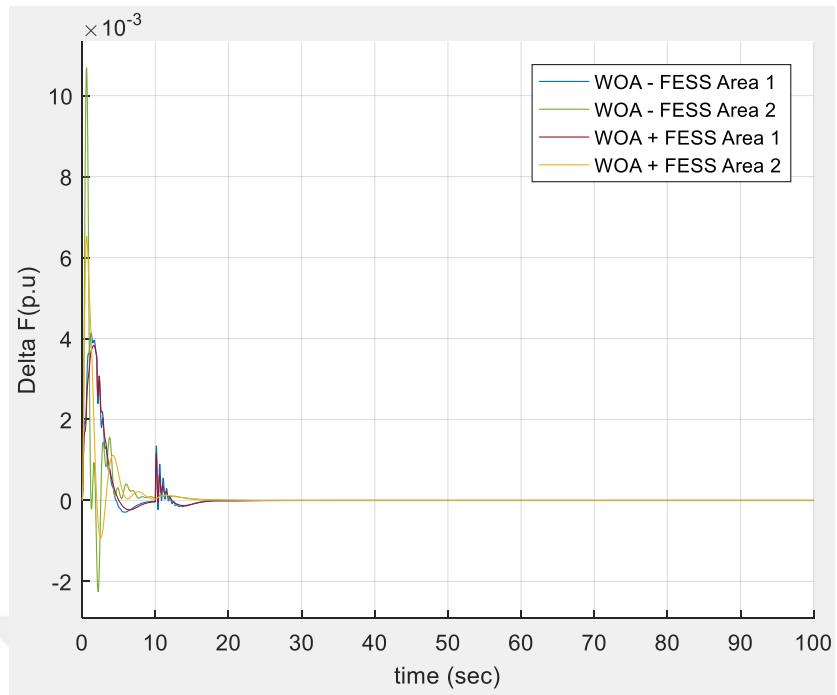


Figure 6.24. Frequency deviation comparison under WOA on charging and discharging of FESS

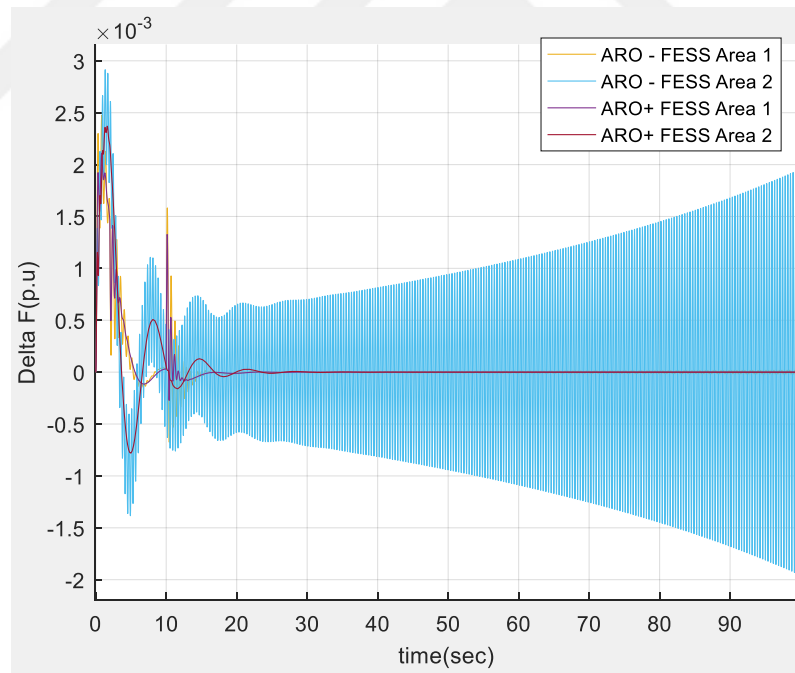


Figure 6.25. Frequency deviation comparison under ARO on charging and discharging of FESS

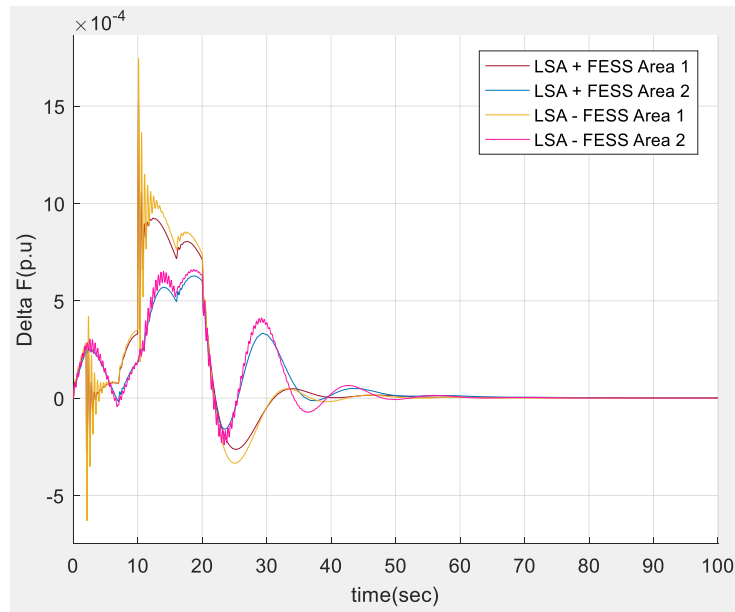


Figure 6.26. Frequency deviation comparison under LSA on charging and discharging of FESS

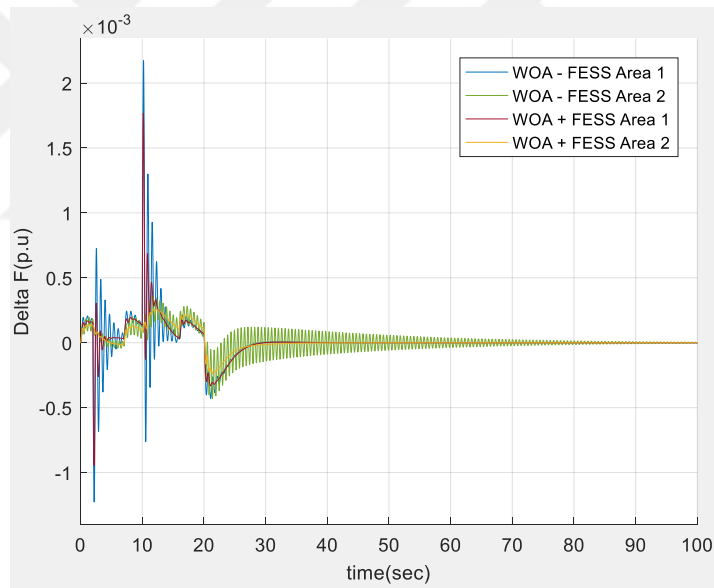


Figure 6.27. Frequency deviation comparison under WOA on charging and discharging of FESS

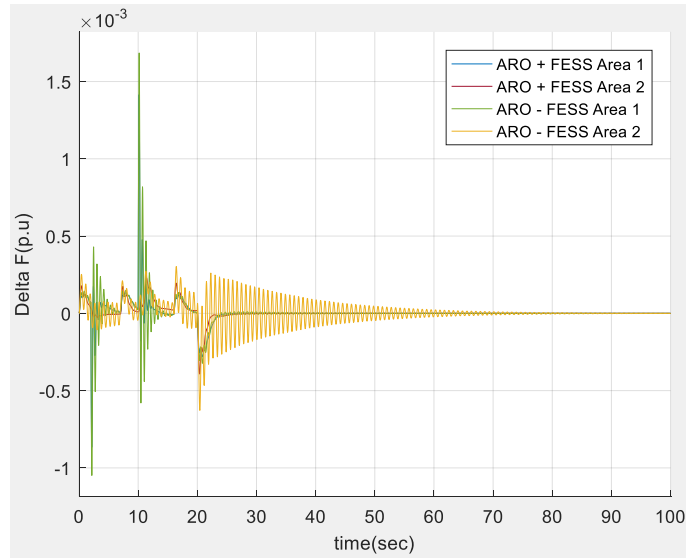


Figure 6.28. Frequency deviation comparison under ARO on charging and discharging of FESS

6.1.9 Case 9

The Simulink model in Figure 6.29 presents the two-area system with ancillary RES as well as the ESSs. A and B indicate area 1, C and D indicate area 2. The results of the simulation were found using the optimized PID parameters under the WOA method and then compared the dynamics of SMESS, FESS, and BESS in the light of parameters drafted in Tables 6.8 and 6.9 corresponding to Areas 1&2. As presented in Table 6.8, FESS on average, showcases a better performance with the shortest settling time of 30.9, a minimum of 0.0012, during the charging as illustrated in Figure A of 6.30, the B part shows the discharging comparison of the ESSs in which the FESS appears to be unsmoothed and less damped. The C shows the Area-2 during the charging with the equivalent parameters of the simulation in Table 6.9. However, the result shows the SMESS to have a better performance on average with the minimum settling time, undershoot, overshoot, ITAE during charging and ITAE during the discharge. In Figure 6.30, in A, the FESS appears to have a smoother signal during the charging and SMESS is less smooth. In B, SMESS shows a damper signal compared to FESS and BESS. In area 2, In C during charging, SMESS shows the smoothest signal and BESS less unlike during the discharge as in D, the FESS appears to be less smooth.

Table 6.8. Comparison of Energy storage performance in Area-1

Types of ESS	Settling Time	overshoot	Undershoot	ITAE During charging	PID values using WOA Optimization	ITAE During discharging
SMES	32.5	0.00097	-0.00051	0.8962	K = 75.4687, I = 33.7123, D = 23.9953	1.084
FESS	30.9	0.001295	-0.000724	0.9264		2.196
BESS	31.5	0.001387	-0.000785	0.9486		1.025

Table 6.9. Comparison of Energy storage performance in Area-2

Types of ESS	Settling Time	overshoot	Undershoot	ITAE	PID values using WOA Optimization	ITAE During discharge
SMESS	42.7	0.000151	-0.000164	0.5707	K = 79.4831, I = 45.8849, D = 47.1088	0.5795
FESS	40.8	0.000161	-0.000193	0.5772		0.6164
BESS	41.6	0.000165	-0.000197	0.5771		0.58

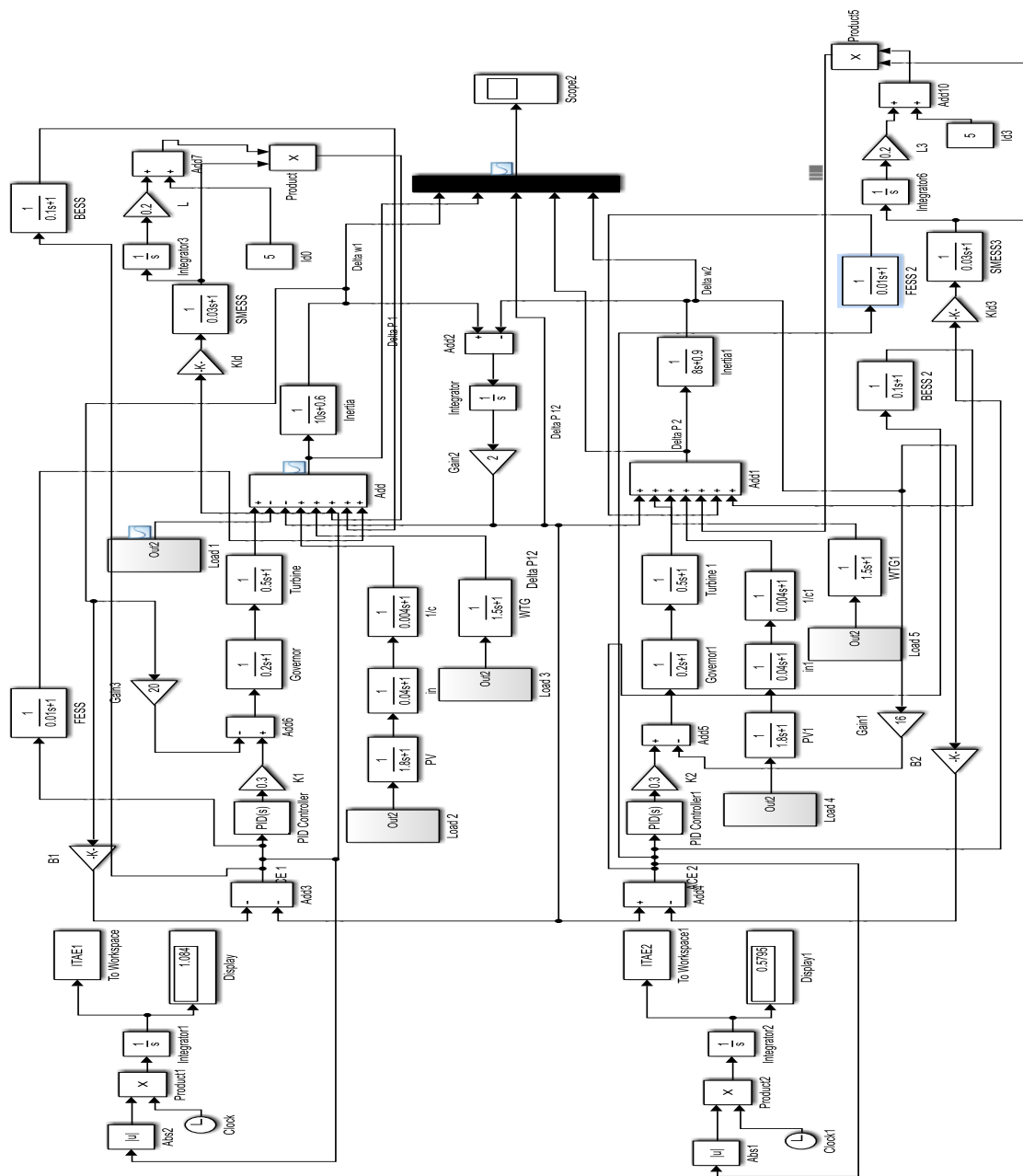


Figure 6.29. Simulink model of two-area system integrated with RES and ESSs

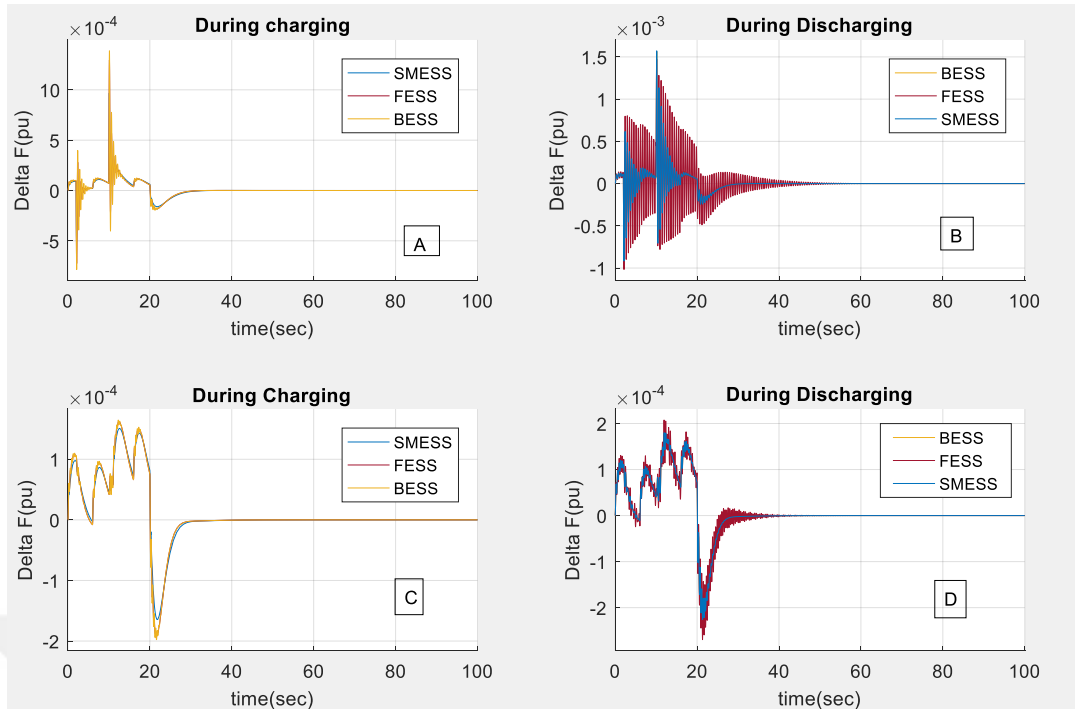


Figure 6.30. Energy storage systems comparison in terms of frequency deviation in Area-1&2

SMESS exhibits the fastest dynamic response with high power output. However, it induces significant oscillations during discharging, which may necessitate additional damping control strategies [37]. BESS provides the most stable and smooth response with minimal oscillations. Due to lower power density, BESS may not be ideal for rapid frequency regulation but is beneficial for long-term energy balancing. FESS offers a balance between power and energy density. It also exhibits moderate oscillatory behavior but has a quicker stabilization time compared to SMESS [38].

This comparison highlights the trade-offs among different ESS technologies in grid frequency regulation. While SMESS offers rapid response, it introduces high-frequency oscillations that require additional control measures [39][40]. BESS provides smooth stabilization but has slower power dynamics. FESS serves as a middle-ground solution. The selection of ESS for power system applications should consider factors such as response time, power density, and damping characteristics to optimize frequency stability [41][42].

6.2 Conclusion

In this chapter, the results of the simulations were arranged in order from simpler single-area system to a two-area system. The case studies demonstrate the

effectiveness of different optimization techniques and energy storage systems (ESS) in enhancing power system stability. ARO consistently outperforms WOA and LSA in minimizing frequency deviations, overshoot, and settling time. The integration of PV and WT introduces challenges, but ARO provides the best overall performance. Among ESS technologies, FESS balances power and energy density with fast stabilization, SMESS offers rapid response but induces oscillations, and BESS ensures smooth frequency regulation with slower dynamics. The findings highlight the importance of selecting appropriate control strategies and ESS technologies for improved grid stability and frequency regulation.



CHAPTER 7

CONCLUSION

This study emphasizes the advantage of effective frequency regulation in modern power systems, especially with the increasing integration of RES such as, PV and WT systems. The variability and uncertainty in RES outputs, together with dynamic load changes, create significant challenges to maintaining system stability. This research evaluates the performance of three optimization methods (ARO, LSA, and WOA) to improve the tuning of PID controllers for frequency control in both single-area and two-area test systems. The findings demonstrate that ARO's superior robustness in mitigating frequency instability caused by severe load perturbations and variable RES inputs. It achieves faster frequency stability and oscillations, ensuring that power output matches the load demand more efficiently. The study further highlights the impact of ESS such as BESS, FESS, and SMESS on system stability. The FESS stands out as the most effective ESS in reducing frequency oscillations and improving transient stability. However, all ESSs introduce a trade-off by increasing the system settling time. The combination of optimized PID control and ESS deployment offers a reliable solution to address the challenges posed by the variability of RES and dynamic load changes in power systems. Simulation results indicate that the operation of both single-area and two-area test systems are improved with optimized PID parameters tuned by ARO method. The two-area system shows improved tie-line power compensation, reduced frequency deviation, and enhanced overall stability under various load and RES disturbances. In scenarios involving dynamic load changes and white noise inputs from WT, the ARO demonstrates resilience by maintaining lower overshoot and undershoot values compared to other algorithms

7.1 Summary of Contributions

The following are the significant contributions of this thesis:

- Emphasize the effectiveness of frequency regulation in the power system, especially due to the increasing integration of RES.

- It explores the impact of ESS on system stability. Henceforth, FESS stands out as the best ESS due to its quick response and durability.
- The benefit of optimization methods in stabilizing the frequency in both single- and two-area systems.

7.2 Future Expectations

Notably, based on the findings and limitations of this study, the future of this work can focus on the exploration of hybrid optimization techniques by combining the ARO with WOA or LSA that could further enhance the tuning of PID controllers and provide better convergence speed, accuracy, and robustness. Since weather uncertainty is a major factor in RES variability, the impact of weather forecasting on frequency regulation can also be further researched by integrating advanced weather forecasting models into frequency control strategies. Accurate predictions of solar irradiation and wind speeds can enhance the effectiveness of the optimization techniques in mitigating frequency disturbance.

REFERENCES

- [1] Marija Maisch (2024) PV Magazine Energy Storage, BNEF: Lithium-ion battery pack prices drop to record low of \$115/kWh - Energy Storage (Accessed date: 26/01/2025)
- [2] America Hernandez (2025) Reuters, TotalEnergies to invest in six German battery-storage projects | Reuters (Accessed date: 26/03/2025)
- [3] U. Akram, M. Nadarajah, R. Shah, F. Milano, A review on rapid responsive energy storage technologies for frequency regulation in modern power systems, *Renewable and sustainable energy reviews* 120 (2020) 109626
- [4] G. Ali, H. Aly, & T. Little, (2024). Automatic generation control of a Multi-Area hybrid renewable energy system using a proposed novel GA-Fuzzy Logic Self-Tuning PID Controller. *Energies*, 17(9), 2000. <https://doi.org/10.3390/en17092000>
- [5] G. El-Saady, E. A. Ibrahim, and A. H. Okilly, "HVDC FACTS Controller for Load Frequency Control System," Conference Paper, January 2018.
- [6] M. Elsis, M. Aboelela, M. Soliman, & W. Mansour, (2018). Design of Optimal Model Predictive Controller for LFC of Nonlinear Multi-area Power System with Energy Storage Devices. *Electric Power Components and Systems*, 46(11–12), 1300–1311. <https://doi.org/10.1080/15325008.2018.1469056>
- [7] M. I. Ibraheem, M. Edrisi, M. Gholipour, & H. H. Alhelou, (2022). A Novel Frequency Regulation in Islanded Microgrid using Sliding Mode Control with Disturbance Observers considering Storages and EVs. *Computers & Electrical Engineering*, 105, 108537. <https://doi.org/10.1016/j.compeleceng.2022.108537>
- [8] L. O. Ibrahim, I. Y. Chung, J. Youn, J. W. Shim, M. Y. Sung, M. Yoon. J. Suh, (2022) Coordinated Frequency Control of an Energy Storage System with a

generator for Frequency Regulation in a power plant, *Sustainability* 2022, 14, 16933

- [9] H. K. Mehta, H. Warke, K. Kukadiya, & A. K. Panchal, (2019). Accurate expressions for Single-Diode-Model Solar Cell Parameterization. *IEEE Journal of Photovoltaics*, 9(3), 803–810. <https://doi.org/10.1109/jphotov.2019.2896264>
- [10] P. K. Ray, & A. Mohanty, (2019b). A robust firefly–swarm hybrid optimization for frequency control in wind/PV/FC based microgrid. *Applied Soft Computing*, 85, 105823. <https://doi.org/10.1016/j.asoc.2019.105823>.
- [11] L. Wei (2018). [dx.doi.org/10.6084/m9.figshare.6025748](https://doi.org/10.6084/m9.figshare.6025748). figshare. Dataset. <https://doi.org/10.6084/m9.figshare.6025748.v1>
- [12] H. Saadat, “Power system control” p.566, (1999). *Power system analysis / Hadi Saadat*. 3rd ed <http://repository.fue.edu.eg/xmlui/handle/123456789/3867>
- [13] S. Gao, C. Xiang, M. Yu, K. T. Tan, & T. H. Lee, (2023). On Solar Photovoltaic Parameter Estimation: Global Optimality Analysis and a Simple Efficient Differential Evolution Method. *IEEE*, 2563–2569. <https://doi.org/10.1109/cdc49753.2023.10383303>
- [14] N. D. Minh, T. T. Chuong, B. Van Huy, Q. D. Cuong & B. D. Thanh, (2019). Research and design of inverter applied in solar PV systems connected to distribution grid. *J Of Electrical Engineering*, 7(1). <https://doi.org/10.17265/2328-2223/2019.01.006>
- [15] S. Singh, S. Saini, S. K. Gupta, & R. Kumar, (2023). Solar-PV inverter for the overall stability of power systems with intelligent MPPT control of DC-link capacitor voltage. *Protection and Control of Modern Power Systems*, 8(1). <https://doi.org/10.1186/s41601-023-00285-y>
- [16] N. N. Minh, T. T. Chuong, B. V. Huy, Q. D. Cuong & B. D. Thanh, (2019b). Research and design of inverter applied in solar PV systems connected to distribution grid. *J Of Electrical Engineering*, 7(1). <https://doi.org/10.17265/2328-2223/2019.01.006>

- [17] S. A. Mata, J. J. P. Martínez, J. B. Quesada, F. P. Larrañaga, N. Yadav, J. S. Chawla, V. Sivaram, & M. F. Howland, (2024). Modeling the effect of wind speed and direction shear on utility-scale wind turbine power production. *Wind Energy*, 27(9), 873–899. <https://doi.org/10.1002/we.2917>
- [18] Y. M. Saint-Drenan, R. Besseau, M. Jansen, I. Staffell, A. Troccoli, L. Dubus, J. Schmidt, K. Gruber, S. G. Simões, & S. Heier, (2020). A parametric model for wind turbine power curves incorporating environmental conditions. *Renewable Energy*, 157, 754–768. <https://doi.org/10.1016/j.renene.2020.04.123>
- [19] F. M., Gonzalez-Longatt, & S. M. Alhejaj, (2016). Enabling inertial response in utility-scale battery energy storage system. *IEEE*, 605–610. <https://doi.org/10.1109/isgt-asia.2016.7796453>
- [20] R. G. H. Tan, & G. K. Tinakaran, (2020). Development of battery energy storage system model in MATLAB/Simulink. *International Journal of Smart Grid and Clean Energy*, 180–188. <https://doi.org/10.12720/sgce.9.1.180-188>
- [21] N. Andrenacci, E. Chiodo, D. Lauria, & F. Mottola, (2018). Life cycle estimation of battery energy storage systems for primary frequency regulation. *Energies*, 11(12), 3320. <https://doi.org/10.3390/en11123320>
- [22] M. M. Rana, M. F. Romlie, M. F. Abdullah, M. Uddin, & M. O. Rahman, (2021). Modeling of an isolated microgrid with hybrid PV-BESS system for peak load shaving simulation. *International Journal of Advanced Technology and Engineering Exploration*, 8(75), 352–361. <https://doi.org/10.19101/ijatee.2020.762168>
- [23] S. Mirjalili, & A. Lewis, (2016). The whale Optimization Algorithm. *Advances in Engineering Software*, 95, 51–67. <https://doi.org/10.1016/j.advengsoft.2016.01.008>
- [24] W. Su, T. Jin and S. Wang, "Modeling and simulation of short-term energy storage: Flywheel," *2010 International Conference on Advances in Energy Engineering*, Beijing, 2010, pp. 9-12, doi: 10.1109/ICAEE.2010.5557629.

- [25] Elbouchikhi, E., Amirat, Y., Feld, G., Benbouzid, M., & Zhou, Z. (2020). A Lab-scale Flywheel Energy Storage System: Control Strategy and Domestic Applications. *Energies*, 13(3), 653. <https://doi.org/10.3390/en13030653>
- [26] S. M. Lukic, J. Cao, R. C. Bansal, F. Rodriguez and A. Emadi, "Energy Storage Systems for Automotive Applications," in *IEEE Transactions on Industrial Electronics*, vol. 55, no. 6, pp. 2258-2267, June 2008, doi: 10.1109/TIE.2008.918390.
- [27] A. K. Sahoo, N. Mohanty & M. Anupriya, (2015). Modeling and simulation of superconducting magnetic energy storage systems. *International Journal of Power Electronics and Drive Systems (IJPEDS)*, 6(3), 524.
- [28] E. A. Gouda, A. Abd-Alaziz & M. El-Saadawi, (2020). Design modeling, and control of multi-stage SMES integrated with PV system. *Journal of Energy Storage*, 29, 101399. <https://doi.org/10.1016/j.est.2020.101399>
- [29] O. N. Oyelade, A. E. Ezugwu, T. I. A. Mohamed & L. Abualigah, (2022). Ebola Optimization Search Algorithm: A new Nature-Inspired Metaheuristic Optimization Algorithm. *IEEE Access*, 10, 16150–16177. <https://doi.org/10.1109/access.2022.3147821>
- [30] H. Shareef, A. A. Ibrahim, & A. H. Mutlag, (2015). Lightning search algorithm. *Applied Soft Computing*, 36, 315–333. <https://doi.org/10.1016/j.asoc.2015.07.028>
- [31] L. Abualigah, M. A. Elaziz, A. G. Hussien, B. Alsalibi, S. M. J. Jalali & A. H. Gandomi, (2020). Lightning search algorithm: a comprehensive survey. *Applied Intelligence*, 51(4), 2353–2376. <https://doi.org/10.1007/s10489-020-01947-2>
- [32] L. Wang, Q. Cao, Z. Zhang, S. Mirjalili & W. Zhao, (2022). Artificial rabbits optimization: A new bio-inspired meta-heuristic algorithm for solving engineering optimization problems. *Engineering Applications of Artificial Intelligence*, 114, 105082. <https://doi.org/10.1016/j.engappai.2022.105082>
- [33] A. E. Khalil, T. A. Boghdady, M. H. Alham & D. K. Ibrahim, (2023). Enhancing the conventional controllers for load frequency control of isolated

microgrids using proposed Multi-Objective Formulation via Artificial Rabbits Optimization algorithm. *IEEE Access*, 11, 3472–3493. <https://doi.org/10.1109/access.2023.3234043>

- [34] S. Banerjee, J. Chatterjee & S. Tripathy, (1990). Application of magnetic energy storage unit as load-frequency stabilizer. *IEEE Transactions on Energy Conversion*, 5(1), 46–51. <https://doi.org/10.1109/60.50811>
- [35] C. Cárdenas-Bravo, D. Dutykh & S. Lespinats, (2024). On the parameters domain of the single-diode model. *Solar Energy*, 277, 112718. <https://doi.org/10.1016/j.solener.2024.112718>
- [36] A. Julius, S. Corigliano, M. Merlo, and Z. Dan BESS Primary Frequency control strategies for West African Power Pool, *Energies* 2022, 15, 990
- [37] X. H. Nguyen & M. P. Nguyen, (2015). Mathematical modeling of photovoltaic cell/module/arrays with tags in Matlab/Simulink. *ENVIRONMENTAL SYSTEMS RESEARCH*, 4(1). <https://doi.org/10.1186/s40068-015-0047-9>
- [38] M. Li, R. Shan, A. Abdullah, J. Tian, S. Gao, High Energy Capacity or High Energy Rating: Which is the more important performance matrix for battery energy storage systems at different penetrations of variable renewables? *Journal of energy storage* 59 (2023) 106560
- [39] V. Patel, D. Guha & S. Purwar, (2019). Frequency regulation of an islanded microgrid using integral sliding mode control. 2019 8th International Conference on Power Systems (ICPS), 1–6. <https://doi.org/10.1109/icps48983.2019.9067402>
- [40] V. V. Yadav, B. Saravanan, Multimachine stability Improvement with hybrid energy renewable system using a superconducting magnetic energy storage in power systems, *journal of energy storage* 57 (2023) 106255
- [41] D. Xie, X. Wei, Y. Ning, S. Yang and Z. Zhou, "Power System Restoration Method With the Flywheel Energy Storage Support," 2023 8th International Conference on Power and Renewable Energy (ICPRE), Shanghai, China, 2023, pp. 1028-1032, doi: 10.1109/ICPRE59655.2023.10353641

- [42] X. P. Nguyen, A. T. Hoang, "The Flywheel Energy Storage System: An Effective Solution to Accumulate Renewable Energy", 2020 6th International Conference on Advanced Computing and Communication Systems (ICACCS), pp.1322-1328, 2020



APPENDIX

Artificial Rabbit Optimization Algorithm

```
function cost = optim(kk)

assignin('base','kk',kk);

sim('Grid3.slx');

cost= ITAE1(length(ITAE1));

cost= ITAE2(length(ITAE2));

end

function [BestSolution, BestFitness] = ARO_OptimSimulink(nRabbits, MaxIter, LB,
UB)

% run_ARO.m: Script to run the ARO optimization for Simulink

% Parameters

nRabbits = 30;    % Number of rabbits (population size)

MaxIter = 50;    % Maximum number of iterations

LB = [0, 0, 0]; % Lower bounds for kk

UB = [10, 10, 10]; % Upper bounds for kk

% Run the ARO algorithm with the Simulink model

[BestSolution, BestFitness] = ARO_OptimSimulink(nRabbits, MaxIter, LB, UB);

% Display results

disp('Optimal Parameters (kk):');

disp(BestSolution);
```

```

disp('Best Fitness:');

disp(BestFitness);

end

function [BestSolution, BestFitness] = ARO_OptimSimulink(nRabbits, MaxIter, LB,
UB)

% Inputs:

% nRabbits - Number of rabbits (population size)

% MaxIter - Maximum number of iterations

% LB, UB - Lower and upper bounds of the parameters (kk)

% Parameters

% Initialize the population

Dim = length(LB); % Dimension of the parameter vector (kk)

Rabbits = repmat(LB, nRabbits, 1) + rand(nRabbits, Dim) .* (repmat(UB - LB,
nRabbits, 1));

Fitness = arrayfun(@(i) optim(Rabbits(i, :)), 1:nRabbits);

% Initialize the best solution

[BestFitness, BestIdx] = min(Fitness);

BestSolution = Rabbits(BestIdx, :);

% Main optimization loop

for iter = 1:MaxIter

% Dynamically update parameters

a = 2 - 2 * (iter / MaxIter); % Exploration to exploitation transition

b = rand; % Random coefficient for movement

for i = 1:nRabbits

```

```

% Generate new positions based on rabbit behavior
if rand < 0.5
    % Exploration: Random hiding behavior
    NewRabbit = Rabbits(i, :) + a * rand(1, Dim) .* (BestSolution - Rabbits(i,
:));
else
    % Exploitation: Detour foraging
    RandomRabbit = Rabbits(randi([1, nRabbits]), :);
    NewRabbit = Rabbits(i, :) + b * (RandomRabbit - Rabbits(i, :));
end

% Apply boundary constraints
NewRabbit = max(NewRabbit, LB);
NewRabbit = min(NewRabbit, UB);

% Evaluate fitness using the optim.m function
NewFitness = optim(NewRabbit);

% Update the rabbit's position if the fitness improves
if NewFitness < Fitness(i)
    Rabbits(i, :) = NewRabbit;
    Fitness(i) = NewFitness;
end

% Update the best solution
if NewFitness < BestFitness
    BestFitness = NewFitness;
    BestSolution = NewRabbit;
end

```

```
end
```

```
end
```

```
% (Optional) Display progress
```

```
fprintf('Iteration %d: Best Fitness = %.6f\n', iter, BestFitness);
```



CURRICULUM VITAE

Profile Summary

Innovative and result-oriented researcher and a master's degree in power systems Engineering (in progress) and about two years of hands-on experience in power system modelling, control, and optimization. I specialize in the integration of renewable energy systems and the development of advanced control strategies for dynamic power systems. Skilled in MATLAB/Simulink with a strong ability to apply innovative problem-solving techniques and conduct rigorous simulations. Dedicated to producing impactful, peer-reviewed and mentoring students in a collaborative academic environment.

Core Competencies

- **Power System Optimization & Modelling**
 - **Voltage Regulation & Stability Analysis**
 - **Renewable Energy Integration (Wind & Solar)**
 - **Energy Storage Systems for Grid Stability**
 - **MATLAB/Simulink Programming & Simulations**
 - **Research Methodologies & Technical Reporting**
 - **Team Collaboration & Independent Research**
-

Work Experience

Researcher on Power Systems Stability and Control

Gaziantep University, Gaziantep, Türkiye
January 2023 – Present

- **Conducted advanced research on frequency regulation to address challenges of renewable energy integration in power systems.**
- **Investigated energy storage solutions to enhance grid stability and improve frequency response under varying operational conditions.**
- **Developed optimization techniques to improve steady-state performance, minimizing transient effects and recovery times.**
- **Designed and validated models in MATLAB/Simulink, simulating fault conditions and assessing control strategies for renewable energy integration.**

Education	Professional Development
<p>MSc in Power System Engineering Gaziantep University, Gaziantep, Türkiye (Expected Completion: February 2025)</p> <p>BSc in Electrical and Electronics Engineering Eastern Mediterranean University, Cyprus (Graduation: June 2018)</p>	<ul style="list-style-type: none">• High Voltage and Insulation Techniques for Electrical Power Systems• Electrical Power Distribution Design (PSCAD)• Advanced MATLAB/Simulink for Electrical Engineering Applications

Research Highlights

- **Frequency Regulation in Renewable Energy Systems: Developed and implemented control strategies to manage frequency fluctuations in grids with high wind and solar energy penetration.**
- **Energy Storage for Grid Stability: Modelled and analyzed energy storage systems to mitigate frequency droop and enhance grid resilience.**
- **Meta-heuristics Optimization Methods: Researched and simulated the newest optimization methods for enhancing PID parameters for better stability in distribution networks under dynamic conditions**

Technical Skills

- **MATLAB/Simulink (Advanced)**
- **Power System Analysis: Renewable Energy Integration, Microgrid Control, Frequency Regulation.**
- **Optimization: PID Parameter Tuning, Control System Design**
- **Technical Reporting and Academic Writing**